Near-real-time service provision during effusive crises at Etna and Stromboli: Basis and implementation of satellite-based IR operations

Peter I. Miller[1] and Andrew J.L. Harris[2]

[1]Plymouth Marine Laboratory, Plymouth, UK

[2]Laboratoire Magmas et Volcans, Université Blaise Pascal, Clermont Ferrand, France

Abstract. Using the NEODAAS-Dundee AVHRR receiving station (Scotland), NEODAAS-Plymouth can provide calibrated brightness temperature data to end users or interim users in near-real time. Between 2000 and 2009 these data were used to undertake volcano hot spot detection, reporting and time-average discharge rate dissemination during effusive crises at Mount Etna and Stromboli (Italy). Data were passed via FTP, within an hour of image generation, to the hot spot detection system maintained at Hawaii Institute of Geophysics and Planetology (HIGP, University of Hawaii at Manoa, Honolulu, USA). Final product generation and quality control was completed manually at HIGP once a day, so as to provide information to onsite monitoring agencies for their incorporation into daily reporting duties to Italian Civil Protection. We here describe the processing and dissemination chain, which was designed so as to provide timely, useable, quality-controlled and relevant information for "one voice" reporting by the responsible monitoring agencies.

Introduction

The 1980's saw a number of studies that used Advanced Very High Resolution Radiometer (AVHRR) mid-infrared (MIR) and long-wave infrared (TIR) data to detect, track and measure the spatial and temporal occurrence of natural fires and anthropogenic hot spots, such as those associated with oil platforms and industry (e.g., Matson and Dozier, 1981; Muirhead and Cracknell, 1984; 1985). In her review, "*Fire from space: Global fire evaluation using infrared remote sensing*", Robinson (1991) listed 14 papers that focused on such efforts using AVHRR data between 1980 and 1989, to which a 15th can be added: the study of Dozier (1980) (Table 1). As part of these efforts, the decade spanning 1985 to 1995 saw the development of a number of algorithms to detect wild fires in AVHRR, as well as GOES-Imager, data. Table 2 flags the paper of Flannigan and Vonder Haar (1986) as the first

publication of an automated fire detection algorithm, where we then tabulate 11 different algorithms developed during following nine years, with a 12th – the "*Contextual algorithm for AVHRR fire detection"* of Flasse and Ceccato (1996) – being published in 1996.

Algorithms used to detect hot spots in satellite-sensor data, as developed by the fire and volcanological communities, can be split into three classes depending on way in which the algorithm defines a hot spot (Steffke and Harris, 2011). Fixed threshold algorithms use single or multiple test and thresholds to determine whether a pixel is hot or not, assessing whether the target pixel's spectral character flags it as anomalously hot. Contextual algorithms assess the pixel's spatial context, using statistics from the target pixel's immediate image background to assess whether the pixel brightness is significantly different from that of its surrounding pixels or not. Finally, temporal algorithms assess whether the pixel brightness is significantly different from that of its proceeding history, thus determining whether a pixel is thermally anomalous in a temporal sense. As a result of the work reviewed in Tables 1 and 2, the fire community had defined the basis of fixed threshold and contextual algorithms by 1995. Of the algorithms collated in Table 2, seven algorithms were fixed threshold and five were contextual. These fire detection algorithms, and their physical basis, underpinned many of the volcanic hot spot detection algorithms that followed. Importantly, the concept of ΔT was established by the fire community, being used by seven of the algorithms of Table 2. That is, the differing sensitivities of the MIR and TIR to a sub-pixel hot spot will mean that the pixel-integrated temperature for the hot-spot pixel will be higher in the MIR than in the TIR. In the example given by Harris (2013), a 2 m radius volcanic vent at 950 °C is set against a 0 °C background in a 1000 m AVHRR pixel, with solar-heated pixels being apparent lower on the volcanoes flanks at 40 °C. For this case, the MIR pixel-integrated temperature (T_{MIR}) is 11 °C, but in the TIR the pixel-integrated temperature (T_{TIR}) is 0.04 °C, i.e., colder than the pixels lower on the volcanoes flanks at 40 °C. However, if we subtract the brightness temperature in the TIR from that in the MIR we have a difference ($\Delta T = T_{MIR} - T_{TIR}$) of ~10 °C. If we take the surrounding solar heated pixels at 40 °C, the temperature will be approximately the same in both wavebands, so that ΔT is ~0 °C. Now, the hot spot that was not resolvable using one waveband of data becomes resolvable using ΔT. That is, it shows up as a value of 10 °C against a flat background of near-zero values.

Based on advances made by the fire community, the first automated detection algorithm for volcanic hot spots, the VAST (Volcanic Anomaly SofTware) code of Higgins and Harris (1997), was introduced in 1995 (Harris et al., 1995a). Written in ANSI C and made generally available through download from the *Computers & Geosciences* web-site, VAST was initially tested on AVHRR data for Etna and later on AVHRR data for Australian wild-fires burning around Sydney (Harris, 1996). VAST was a

contextual algorithm that used ΔT. Shortly thereafter, the first temporal algorithm – the Robust AVHRR Techniques (RAT) algorithm – came on-line (Tramutoli, 1998). Later renamed the Robust Satellite Technique (RST) the algorithm relied on an archive of MIR data to create an Absolutely Local Index of Change of Environment (ALICE) (Pergola et al., 2008; 2009). ALICE provided an estimate of how much a pixel brightness diverged from its normal conditions as determined from the data time series, normalized for its natural variability in the time domain so as to detect temporally anomalous behavior including volcanic hot spots (e.g., Di Bello et al. 2004). In 2000, the now widely-used MODVOLC system became operational (Flynn et al., 2002; Wright et al., 2002). Based on a detection routine that used a fixed threshold algorithm based on the ΔT principle, the normalized thermal index (NTI), MODVOLC provided a simple global hot spot detection capability that required a minimal number of mathematical operations (Wright et al., 2002; 2004). Thus, as of 2000, a number of volcano hot spot satellite-sensor detection and reporting systems were operational, including the Okmok algorithm (Dehn et al., 2000). This was developed at the Alaska Volcano observatory (AVO) to aid with operational hot spot detection in AVHRR data. As part of the AVO function, over 100 volcanoes across Alaska, the Aleutians, Kamchatka, and the northern Kurile islands were monitored in as close-to-real-time-as-possible using direct reception of AVHRR, GOES and GMS data at a receiving station installed at the University of Alaska (Fairbanks) in 1990 (Dean et al., 1996; 1998). We here explore the implementation and utility of an operational satellite-sensor based hot spot detection and tracking system launched in 2000 and still, like the MODVOLC system, operational today.

The Natural Environment Research Council (NERC) Earth Observation Data Acquisition and Analysis Service (NEODAAS) is funded by NERC to support UK research scientists with remote sensing data (http://www.neodaas.ac.uk/). The service has the capability to automatically receive, process, and archive data from multiple polar-orbiting sensors, including MODIS and AVHRR, in near-real time. Data are also received and processed from multiple geostationary satellites, including SEVIRI, VISSR, GOES and MTSAT (Groom et al., 2006). Between 2000 and 2009, AVHRR data supplied in near-real time by NEODAAS were used to communicate hot spot information during effusive crises at Mt. Etna and Stromboli (Italy). We here describe this data reception, processing and communication chain.

The satellite data: reception and pre-processing

The NEODAAS service is hosted at two sites. While data reception and acquisition is provided by the Dundee Satellite Receiving Station at the University of Dundee (NEODAAS-Dundee), data processing is provided by the Remote Sensing Group at the Plymouth Marine Laboratory (NEODAAS-Plymouth).

NEODAAS-Dundee

During the 1970s, an AVHRR receiving station was developed at the University of Dundee. Data were archived onto magnetic tapes and a quick-look image archive was maintained, and updated daily, in a photographic format filed in ring-binders. During the 1990s raw data could be ordered on magnetic tape, but delivery delays were of the order of weeks. However, archived AVHRR data were used to:

1. Test initial hot spot detection algorithms (Harris et al., 1995a; Pergola et al., 2001);
2. Track effusive eruptions through spatial and temporal analysis of spectral radiance (Harris et al., 1995b, 1997a; Tramutoli et al., 2001);
3. Develop means for time-averaged discharge rate extraction (Harris et al., 1997b; Harris and Neri, 2002); and
4. Define and understand detector response problems over high temperature targets (Setzer and Verstraete, 1994; Harris et al., 1995c).

All data received by NEODAAS-Dundee are processed in near-real time and made available on-line. These are automatically added to the online archive, whose sensor and data base coverage is summarized in Table 3. Currently, AVHRR, MODIS and MSG data are received directly at NEODAAS-Dundee and two products are generated:

- Level 0: unprocessed instrument data;
- Level 1: geolocated unprocessed instrument data including calibration parameters.

For AVHRR, coverage extends from Newfoundland to Moscow and from North Africa though Greenland (Figure 1a). Image frequency depends on location (Figure 1b), with up to five images a day being available for Etna, although at-least two may be close to the scan edge and, although useful for event detection, are potentially difficult to use quantitatively (Harris et al., 1997b).

NEODAAS-Plymouth

During the 1990s, the Plymouth Marine Laboratory (at the time operating under the auspices of the Remote Sensing Data Analysis Service) provided calibration coefficients for conversion from DN to spectral radiance, upon agreement. Also provided were on-board blackbody temperatures,

necessary for non-linear correction of the conversion. Today, direct-broadcast data received at Dundee are transferred over the internet to Plymouth where higher level processing is undertaken. AVHRR data are processed into sea-surface temperature following Miller et al. (1997), and MODIS data are processed into ocean color and atmospheric products (Shutler et al., 2005); typically 1-2 hours after reception (Groom et al., 2006). Global coverage is available from NASA and ESA sourced data and from geostationary archives for Meteosat, MSG, IODC, GOES-East, GOES-West and MTSAT. Data are processed to provide three further levels of product:

- Level 2: derived variables, such as vegetation indices, sea surface temperature, ocean color and atmospheric properties;
- Level 3: temporally or spatially binned level 2 data, such as daily, weekly or monthly composites for a single product or region;
- Level 4: derived from multiple measurements or models – e.g., ocean front analyses.

Third party (user-specified) products can also be generated. Quick look browse of all products are made available via the internet as quickly as possible, with ftp access to products and data being made available to registered users at the same time.

Data sets for hot spot detection: The role of AVHRR

Across the infrared spectral region (0.7 – 20 µm) there are eight atmospheric windows within which atmospheric transmission is greater than 90 % (Table 4). Hence, wavebands for Earth-surface thermal applications need to be placed in these spectral regions if the surface emission properties are to be measured from the in-orbit location (i.e., above the top of the atmosphere). Following Wein's displacement law, channels placed in the MIR, between 3.44 and 4.13 µm, and in the TIR, between 8.6 and 12.2 µm, will be most sensitive to surfaces at elevated temperatures (fires and active lavas) and typical Earth surface ambient temperatures, respectively (Table 4). The two wavebands have thus respectively been used for measurements of the two surface types, with the extreme sensitivity of the 3.44 to 4.13 µm waveband to sub-pixel hot spots meaning that it has become informally termed the "fire channel" (e.g., Vermote et al., 2009).

AVHRR's channel 3 has been long known to be extremely sensitive to, and thereby capable of, detecting small, high temperature sub-pixel heat sources, such fires due to straw burning and gas flares on oil platforms (Matson and Dozier, 1981; Muirhead and Cracknell, 1984; 1985). However, AVHRR's channel 3 also has a saturation temperature of between 50 and 60 °C, so that data saturate

quite easily over sub-pixel fire and volcanic hot spots (Setzer and Verstraete, 1994; Harris et al., 1995c). Solutions have, though, been found to work around this problem and unsaturated thermal data are usually available over hot spots in AVHRR's two TIR, channels 4 (10.3 – 11.3 µm) and 5 (11.5 – 12.5 µm). In addition, AVHRR data represent the longest continuous meteorological satellite data set, with the NEODAAS MIR and TIR archive dating back to the first launch of AVHRR on TIROS-N in October 1978. If we consider the AVHRR's predecessor, the Very High Resolution Radiometer, the TIR data set can be extended back to first launch on NOAA-2 in November 1972 (Cracknell, 1997). As of 2015, these archives potentially provided a 43-year-long base-line data set, which for equatorial targets has a nominal temporal resolution of four images per day, increasing to 10 or more towards the poles due to convergence of orbits (Harris et al., 1999). Pixels increase in size from, for channel 3B on NOAA's -15, -16 and -17, 1.11 km and circular at nadir to 7.9 × 2.6 km (oblate ellipse) at the edge of the 3000 km wide scan. Pixels will also undergo distortion, become rotated, and become heavily overlapped towards the edge of the ±55.4 ° wide swath. However these effects can be assessed and corrected for (Harris, 2013). Because of AVHRR's utility and longevity, as of 2005 AVHRR accounted for 47 (or 39 %) of the 120 studies published within the field of satellite-sensor based detection, tracking and measurement of volcanic hot spots since 1965 (Harris, 2013).

As Robinson (1991) pointed out, although AVHRR was designed for meteorological observations, channel 3 was somewhat "serendipitously well placed" to detect hot spots. However, the utility of 1-km satellite-based measurements in the MIR for fire and volcano hot spot studies have led to some sensors, such as MODIS and BIRD, being designed with a high gain setting channel at 3.9 µm (that saturates at temperatures of up to 400-450 K) with the fire community specifically in mind (e.g., Kaufman et al., 1998; Wooster et al., 2003). In addition, 3.9 µm channels on geostationary satellites, such as the Imager on GOES and SEVIRI on Meteosat, have long proved capable of tracking hot spots due to fires at temporal resolutions of 15 minutes or better, in-spite of having 3-4 km pixels (e.g., Prins and Menzel, 1994; Roberts and Wooster, 2008). Consequently, the high temporal resolution and "fire channel" detection capability offered by sensors mounted on geostationary platforms have proved to be of extreme utility for shot-lived effusive events or activity varying over time-scales of 10's of minutes, such as activation and deactivation of active fissure segments (e.g., Harris et al., 1997c; Harris and Thornber, 1999; Ganci et al., 2012). Such events may be missed, or just imaged once or twice, by the polar orbiters that carry sensors with thermal capabilities which have return a period of 6-12 h. As a result, today, although NOAA NESDIS (2015a) state that the objective of the AVHRR instrument is to:

> "provide radiance data for investigation of clouds, land-water boundaries, snow and ice extent, ice or snow melt inception, day and night cloud distribution, temperatures of radiating surfaces, and sea surface temperature;"

added is:

> "In addition, land use applications of the AVHRR include monitoring of: food crops; **volcanic activity**; forest fires; deforestation; vegetation; snow cover; sea ice location; desert encroachment; icebergs; oil prospecting and geology applications. Other miscellaneous AVHRR applications include the monitoring of: migratory patterns of various animals; animal habitats; environmental effects of the Gulf War; oil spills; locust infestations; and nuclear accidents such as Chernobyl."

Thus, volcano monitoring has become established and recognized as part of the application of NOAA NESDIS data. In this regard, following NOAA NESDIS (2015b), NESDIS is currently,

> "dedicated to providing timely access to global environmental data from satellites and other sources to promote, protect and enhance the Nation's economy, security, environment and quality of life."

In terms of compatibility with volcano monitoring, the NOAA NESDIS mission is to (NOAA NESDIS, 2015b):

(i) manage operational environmental satellites,

(ii) operate the NOAA National Data Centers,

(iii) provide data and information services including Earth system monitoring,

(iv) perform official assessments of the environment, and

(v) conduct related research.

AVHRR will thus likely continue to be a robust and reliable resource for volcano hot spot monitoring for the fore-seeable future, providing a data base that has its foundations in 55 years of technological and applicative development. As of 2015, six AVHRR sensors were in orbit aboard NOAA's -14 through -19. Although "old", the first satellite in the series having been launched on 1 April 1960 carrying the Vidicon sensor (Cracknell, 1997), the series is by no means obsolete, and is constantly being upgraded,

215 "to support a complete meteorological payload plus the necessary support subsystems to
216 meet all interface and system requirements" (Robel, 2009).

217 At the same time,

218 "NOAA has tried to keep the changes to a minimum" (Robel, 2009)

219 so as to maintain the continuity of service and the "digital archive of data collected from the current
220 generation of NOAA operational polar orbiting satellites" (Kidwell, 1998).

221 The series thus provides a reliable MIR and TIR data set adding, at minimum, four extra 1-km spatial
222 resolution observation data points to an ensemble-based approach that can over up to 16 "looks"
223 per day if we combine NOAA+METOP+TERRA+AQUA capabilities (Harris et al., 2015). What's more,
224 the service us underwritten by NOAA, providing continuity of data and a reliable resource.

225

226 **Tools used for hot spot tracking**

227 AVHRR data provided by NEODAAS-Plymouth for Italy and Iceland were ingested into the Hawaii
228 Institute of Geophysics and Planetology (HIGP) hot spot tracking system. From 2000 onwards, the
229 system ingested near-real time GOES-Imager data to track hot spot activity around the Pacific Rim
230 (Harris et al., 2000a; 2001; 2002a; 2002b), and was linked to the MODVOLC tool. The system
231 produced a number of quick-look image products. These were generated on-the-fly so as to reduce
232 storage space, meaning that only raw data were saved, and then used to generate products from the
233 archive. A rolling text-file data base, containing basic locational and radiance data for each target
234 region of interest (ROI) was also updated with each image acquisition. The same system
235 automatically generated an email notice if the probability of any pixel in a ROI exceeded a threshold,
236 linking the recipient to the image products for image that generated the notice (Harris et al., 2002a).
237 This initial threshold was based on a multistep, fixed threshold approach (Table 5) which operated
238 along the lines of the fire detection algorithms given in Table 2. For the NEODAAS-Plymouth AVHRR
239 data, this algorithm was used purely for issuance of email notices which the recipient used to check
240 the veracity of a "detected" hot spot. If the hot spot was valid, then the operator proceeded
241 manually by checking all images to precedent to the notice so as to ascertain the exact start time
242 (within the temporal resolution of the sensor) of the event. Operator analysis continued by checking
243 each new image until the event was over. Manual checking initially involved detecting and logging
244 anomalous pixels by eye. Later hot pixel detection and selection was guided by application of an up-
245 dated version of VAST. Pixel radiance values were then converted to useable (by the field

246 volcanologist and hazard responder) metrics in a timely fashion, these metrics primarily being time
247 and Time-Averaged Discharge Rate (TADR).

248

249 Manual checking: NEODAAS-Plymouth quick-look hot spot tool

250 NEODAAS-Plymouth maintains a quick-look hot spot tool at
251 https://www.neodaas.ac.uk/supportedscience/etna.php (Figure 2). The tool involves an enhanced
252 AVHRR channel 3 image of Sicily (including the Aeolian Islands) and Iceland. Enlargements of both
253 the channel 3 and channel 4 images for Etna are inset into the overview image. The most recent
254 image is given, along with all images acquired during the preceding week. The current image is
255 updated as soon as new data arrive, and the archive can be browsed using forward and backward
256 buttons at the top of the tool. This simple, but effective, system allows the presence of thermal
257 anomalies to be checked by virtue of their intense radiance in channel 3 and, if sufficiently intense, in
258 channel 4 also, as in the case given in Figure 3.

259 As argued by Harris (2013), visual detection using time series of such images remains the most
260 powerful and trustworthy tool for hot spot detection and tracking. That is,

261 > "by examining multiple images of the same volcano target we train a powerful neural
262 > network for hot spot detection. In some subtle detection cases it may even be difficult for
263 > the operator to describe the detection algorithm they have sub-consciously developed, for
264 > the detection is based upon the most complex of neural networks."

265 In the case of Figure 3, the presence of hot spots due to volcanic activity on Mt. Etna is immediately
266 apparent to the eye. Hence, manual checking – and tools that allow such interaction – remain the
267 most bullet-proof way to ensure that: (i) the hot spot is valid, (ii) all pixels required for complete
268 quantitative analysis are selected, and (iii) no spurious pixels are included.

269

270 Automated checking: VAST-II

271 VAST's implementation is based on the concept of "*natural variation*" (Harris et al., 1995a). This was
272 defined as the difference between a pixel's brightness and that of its surroundings, as defined by the
273 eight pixels immediately surrounding the target pixel (Figure 4). Although over thermally
274 homogeneous surfaces, such as the sea, natural variation should be close to zero; over thermally
275 heterogeneous surfaces, natural variation should be highly variable (and typically greater than 10 °C).

The updated version of VAST used to guide pixel selection in NEODAAS-Plymouth AVHRR data functioned in the same way as the original version, but used the TIR brightness temperature (T_{TIR}) image, rather than the ΔT image, a modification which allowed application when MIR data was lacking. The new version of VAST also allowed user interaction so that anomalous pixels not flagged by the algorithm could be selected or false positives de-selected (Steffke and Harris, 2011).

A 30 × 30 AVHRR pixel target window was centered at 37.37°N, 15.00°E, the size of which could be altered by the operator. Natural variation (ϖ) was then defined for all pixels in the image. An image-specific natural variation threshold (ϖ_{thresh}) was set from the "non-volcanic" portion of the sub-image, this being a 5 pixel wide strip running around the target window, the size of which could also be enlarged or reduced by the operator. The value for ϖ_{thresh} was set equal to the maximum ϖ found within the "non-volcanic" zone. Then, if ϖ for a pixel in the target window was greater than ϖ_{thresh}, it was flagged as anomalous. For pixels at the center of a large anomaly ϖ might be quite low due to all surrounding ΔT or T_{TIR} values being high. Thus, anomalous pixels located in the first run were masked, the ϖ value for each pixel recalculated with hot pixels flagged in the first run excluded, and the test re-run. This process was iterated until no new pixels were found (Harris et al., 1995a). Location and spectral radiance vales for detected pixels – as confirmed, rejected or added by the operator – were then exported to a data file and used for conversion to TADR.

Conversion to TADR

Following Wright et al. (2001), lava area obtained from satellite-sensor IR data can be converted to time-averaged discharge rate following a linear relation:

$$TADR = x\, A_{lava} \quad (1)$$

A_{lava} being the area of active lava, and x being the slope of the linear relation between TADR and A_{lava} for the case in hand (Harris and Baloga, 2009). The satellite-data-derived variable in this relation is A_{lava}, which we derived as follows:

1. AVHRR channel 3 and channel 4 spectral radiances $R_{3\text{-int}}$ and $R_{4\text{-int}}$) were recorded for all detected hot spot pixels (Figure 5).
2. Atmospheric and emissivity corrections were applied to all selected radiances, i.e.,

$$\text{In channel 3: } R_{3\text{-int-corr}} = (R_{3\text{-int}} - R_{reflec}) / \varepsilon_{\lambda 3}\, \tau_{\lambda 3} \quad (2a)$$

$$\text{In channel 4: } R_{4\text{-int-corr}} = (R_{4\text{-int}} - R_{upwell}) / \varepsilon_{\lambda 4}\, \tau_{\lambda 4} \quad (2b)$$

In which ε and τ are the surface emissivity and atmospheric transmissivity in the two wavebands centered at wavelengths $\lambda 3$ and $\lambda 4$, respectively. R_{reflec} is the surface reflected spectral radiance that contributes to the at-sensor pixel-integrated spectral radiance in channel 3, and R_{upwell} is the atmospherically-emitted spectral radiance that contributes to the at-sensor pixel-integrated radiance in channel 4.

3. For each hot spot pixel, a background radiance (R_{back}) is selected from the nearest, non-hot spot, pixel of lowest radiance (Figure 6).
4. Because AVHRR channel 3 is usually saturated over a volcanic (or fire) hot spots (Harris et al., 1995c), only one channel is useable – channel 4 (i.e., $R_{4\text{-}int}$ and $R_{4\text{-}back}$; which when corrected for emissivity and atmospheric effects are $R_{4\text{-}int\text{-}corr}$ and $R_{4\text{-}back\text{-}corr}$). Thus we are forced to apply a one-waveband method (Harris et al.1997a,b; Harris, 2013) so that channel 4 spectral radiances are used in a two component mixture model to obtain the portion of the pixel occupied by the hot source (p):

$$p = (R_{4\text{-}int\text{-}corr} - R_{4\text{-}back\text{-}corr}) / (R_{4\text{-}hot} - R_{4\text{-}back\text{-}corr}) \quad (3)$$

in which $R_{4\text{-}hot}$ is the spectral radiance emitted by the hot (active lava) source resident in the pixel. Due to uncertainty and real variability in the exact value of $R_{4\text{-}hot}$, this value has to be assumed over a range, where the spectral radiance equivalents of the temperature limits 100 °C and 600 °C have been found appropriate for active lava at Etna, Stromboli and Iceland (Harris et al., 2007; Harris and Baloga, 2009; Harris, 2013). This gives two values for p:

(i) a maximum value (p_{max}) obtained with the low temperature assumption (T_l),

(ii) a minimum value (p_{min}) obtained with the high temperature assumption (T_h).

5. Next, pixel area (A_{pixel}) is calculated as a function of scan angle. This is multiplied by p_{max} and p_{min} to obtain a range of estimates for the area of active lava resident in the pixel ($A_{lava\text{-}p}$):

$$A_{lava\text{-}p\text{-}max} = p_{max} A_{pixel} \quad (T_l = 100\ °C) \quad (4a)$$

$$A_{lava\text{-}p\text{-}min} = p_{min} A_{pixel} \quad (T_h = 600\ °C) \quad (4b)$$

Results for all hot spot pixels are summed to obtain a maximum and minimum bound on the total area of active lava at the imaged eruption site ($A_{lava\text{-}max}$ and $A_{lava\text{-}min}$).

6. Finally, to obtain the limits on TADR, the two lava area estimates are placed into two empirically-derived conversion routines tailored for the case in hand (Harris et al., 2010). For the period 2000-2009 at Etna the following conversions were found to

produce the best-empirical fit between model output and ground truth (Harris et al., 2011):

$$TADR_{min}\ (m^3\ s^{-1}) = 5.5 \times 10^{-6}\ (m\ s^{-1})\ A_{lava\text{-}max}\ (m^2) \qquad (T_l = 100\ °C) \qquad (5a)$$

$$TADR_{max}\ (m^3\ s^{-1}) = 150 \times 10^{-6}\ (m\ s^{-1})\ A_{lava\text{-}min}\ (m^2) \qquad (T_h = 600\ °C) \qquad (5b)$$

For Stromboli, we obtained (Calvari et al., 2005):

$$TADR_{min}\ (m^3\ s^{-1}) = 2.5 \times 10^{-6}\ (m\ s^{-1})\ A_{lava\text{-}max}\ (m^2) \qquad (T_l = 100\ °C) \qquad (6a)$$

$$TADR_{max}\ (m^3\ s^{-1}) = 166 \times 10^{-6}\ (m\ s^{-1})\ A_{lava\text{-}min}\ (m^2) \qquad (T_h = 600\ °C) \qquad (6b)$$

Uncertainty

Two TADR values are thus output: one each for the maximum and minimum bound on the derived A_{lava} which, in turn, results from uncertainty in (or impossibility of) applying a single temperature value to describe the thermal surface structure of the lava active within the pixel. As is standard, the uncertainty range lies between the highest possible temperature that can realistically be assigned to this source (T_h) and the lowest (T_l). If the conversion is appropriately set and applied, output TADR have been shown to span the range of field-based estimates (Calvari et al., 2005; 2010; Harris et al., 1997a,b; 2007; 2011; Harris, 2013), while also (on occasion) giving a smaller range of uncertainty than field-based estimates made under similar, near-real time, requirements (e.g., Harris and Neri, 2002).

The range of uncertainty on the satellite-derived TADR is quite large (of the order of ±60 %); but no current near-real time (even post-mortem) lava flux rate measurement method is without its problems, and all can have large error of ~50 % (Harris et al., 2007). Even the careful, but time-consuming, post-emplacement volumetric measurements made of Etna's 1991-1993 lava flow field Stevens et al. (1997) gave (4 years after the event ended) a mean output rate with an uncertainty of 12.5%. Uncertainty and error on TADT measurements is an old problem, which still needs to be addressed. The key challenge remains: how do we make regular, and trusted, TADR measurements in near-real time with uncertainties that are less than 10%? That being said, satellite-derived TADR estimates with 50-60% uncertainty have been proved adequate for tracking effusive events, providing time-series sensitive to real changes in output rate (e.g., Harris et al., 1997a,b; 2000b; 2010), so as to provide output of use in a monitoring and modeling role (e.g., Bonaccorso et al., 2015; Vicari et al., 2009; 2011).

In the case of Stromboli, validated satellite-derived TADR were particularly useful, inspire of large uncertainty, due to (Harris et al., 2005; Calvari et al., 2007; Lodato et al., 2007):

(i) difficulty and danger of access to the active lava flow field, which was emplaced on a steep slope receiving rock fall and hot grain flow from the collapsing lava flow fronts;

(ii) the braided nature of the channel and tube system, and multiplicity of sources;

(iii) a lava emplacement mechanism that eroded the loose substrate on which the flows were emplaced so that lava units became embedded in the surrounding terrain – so that thickness measurements were difficult to make; the location of the flow base being impossible to obtain;

(iv) lava flow instability, where flows were constantly collapsing into the sea, so that emplaced lava units never remained in place for more than a few hours so that post-mortem field-based area (A) and thickness (h) measurements were impossible – Meaning that TADR derivation from Ah/t, t being duration of unit emplacement were likewise impossible on a regular, operational, basis.

TADR tracking using NEODAAS data during effusive crises at Etna and Stromboli

Beginning in 2000, through collaborative agreement with NEODAAS, calibrated, geo-referenced AVHRR channel 3, 4 and 5 brightness temperature data were made available to HIGP for tiles covering Sicily and Iceland (Figure 7). Data were placed on the NEODAAS-Plymouth ftp site upon generation of the brightness temperature image product. A routine running at HIGP checked the ftp site every minute, downloading any new data found. In this way a mirror archive for these two volcanically active zones was built as part of the HIGP hot spot monitoring system.

Because no algorithm can be 100% trusted to select all anomalous pixels 100% of the time (Steffke and Harris, 2011), and so as to be sure that all images used were free of cloud contamination, we preferred a manual approach. Also, because only around five images were received each day, the task of image checking and processing was manageable by a human operator. The task was more daunting when using the 96 GOES images received per day by the system for active targets in the GOES footprint; but manageable by an individual charged with maintaining the system. Such a philosophy ensured product quality control and accountability.

As described by Moxey et al (2003), operators at HIGP would check the archive at 07:00 am (Hawaiian Standard Time) every morning. All new data would be checked, manually, for cloud cover and presence of a hot spot. The radiances of any hot pixels and their cold background were logged and used to convert to time-averaged discharge rate. For a day's worth of AVHRR data, this process would typically take less than 30 minutes. New vales were appended to a summary table which also

contained comments on image quality (e.g., Table 6). This was sent to a controlled email distribution list that involved the main monitoring actors, which included INGV-Catania for eruptions on Etna (Bonaccorso et al., 2015), as well as University of Florence for operations on Stromboli. A hot spot summary table was also maintained (e.g., Table 7). These Tables were appended to a daily up-date email giving, in a standard and consistent format, details regarding the number of images checked, their quality and any TADRs that could be derived (e.g., Table 8).

During Etna's 2001 and 2003 eruptions, as well as during Stromboli's 2002-2003 and 2007 eruptions, TADRs were checked against field measurements to allow an assessment of their reliability (e.g., Figure 8). Results indicated that the empirical conversion applied, that is the x value used in Equation (1), was valid and gave results that agreed with ground-based values (see, for example, Calvari et al. 2005; 2010). In addition, the empirical equation of Calvari and Pinkerton (1998) that relates flow length (L) to TADR,

$$L = 10^{3.11} \times TADR^{0.47} \quad (7)$$

was applied. For the maximum TADR obtained by AVHRR during Etna's 2001 south flank eruption (30 $m^3\ s^{-1}$), this gave a length of 6370 m and compared with a final length of 6.5 km. During the 2001 eruption, this assessment was particularly important because flows were advancing towards the towns of Nicolosi and Belpasso (Figure 9), which lay just a few kilometers further down slope from the flow front (Bonaccorso et al., 2015) and accounted for a total population of 6,959 plus 23,606 for the two population centers, respectively (ISTAT, 2008).

Less useful were the 1 km hot spot location maps, because the location of the lava flows was already well-known by ground observers. The maps, though, were posted on the HIGP hot spots web-site (http://goes.higp.hawaii.edu/goes/etna/) as soon as data had been received from NEODAAS-Plymouth in case of need. Three of these location maps (in raw, labeled and DEM-merged format) are given in Figure 9, and allow – in spite of the 1 km precision – hot spot location to be assessed in relation to vulnerable locations.

Stromboli: Operations case-study

All eruptions at Etna during the period 2000-2009 were tracked as part of the NEODAAS-HIGP collaboration, and the resulting data base for Etna is given in Harris et al. (2011). No effusive eruption occurred in Iceland over the time period of operations, although two major effusive crises occurred on Stromboli during 2002-2003 and 2007. During the 2002-2003 crisis we were invited, by

the Italian Civil Protection Department (DPC), to provide methodologies for timely delivery of TADR (Harris et al., 2003). The site conditions, as already discussed, meant that implementation of ground-based methodologies to deliver TADR were difficult-to-impossible. As a result, by May 2003, after five months of effusive activity only one or two field-based measurements of TADR were available. DPC, however, recognized the value of the near-real time TADR metric in tracking the eruption, and so were eager to develop a means of up-dating TADR time-series on at-least a daily basis.

Initially, a routine to obtain TADR from thermal camera data obtained during the routine helicopter over-flights made at 09:00 (local time) each morning was developed (Harris et al., 2005). Results were delivered, by 10:00 each morning, to DPC (Harris et al., 2003). In parallel with this, TADR were derived from all available (AVHRR and MODIS) satellite resources and added to the daily report, so as to allow an assessment of whether lava output was stable, increasing or decreasing. During 31 May to 16 June 2003 these were given as power-point presentations each evening at 18:00, during the daily DPC briefing held at the COA (Centro Operativo Avanzato) – the on-site operations center (Bertolaso et al., 2009).

Thereafter, the same operation protocol was followed. That is, TADR were prepared on a daily-basis from satellite-flown sensors and then delivered in time for inclusion in daily reporting to DPC. The same protocol was followed during the 2007 crises and involved delivery of TADR reports to members of the Scientific Synthesis Group (SSG). This group was set up under the auspices of DPC (Barberi et al., 2009),

> "to evaluate the scientific aspects of a volcanic emergency, recommend improvements of the surveillance and provide advise and suggestions to the Civil Protection on the appropriate urgent actions to be undertaken to mitigate risks."

The SSG appointed for the 2007 eruption of Stromboli included groups involved in operational monitoring at Stromboli – mainly from INGV or the University of Florence (UNIFI). These groups were also charged with scientific reporting before, during and after the effusive crisis (Bertolaso et al., 2009). We thus passed information to INGV and UNIFI so as to ensure appropriate injection into the response protocol as given in the flow chart of Bertolaso et al. (2009). Based in this experience, and other interactions with local volcano monitoring agencies around the Pacific Rim (Harris et al., 2002a), we developed the internal protocol charted in Figure 10 for information communication; this preventing crossing of communication lines and protocols set-in place by the responding agencies.

Conclusion

NEODAAS-Plymouth has extensive expertise in processing satellite data for sea surface temperature and ocean color, as well as near-real time processing of Earth observation data for volcano monitoring. The primary focus is on processing of data from polar orbiting (medium spatial resolution) sensors (~1 km). Product provision focuses on the needs of the UK academic research community, NEODAAS being funded by NERC to support UK research efforts. However, support can be provided to non-UK applications through agreement.

In the case followed here, through memorandum of understanding, calibrated, geo-referenced brightness temperature images covering Etna, Stromboli and Iceland were provided in near-real-time for ingestion into the HIGP hot spots system. For the July-August 2001 eruption of Etna, as well as Stromboli's 2007 eruption, event onset was alerted to by the automated detection algorithm linked to a hot spot email notice [see Harris et al (2002a) for notice format]. Veracity of the detection was checked through immediate communication with institutes formally responsible for monitoring Etna and Stromboli who, in turned worked with Civil Protection and were mandated to provide information during eruptive crises. Products were prepared and delivered on a daily basis by 18:00 (local – Italian – time). This meant that results when ready for use in daily reporting meetings with Civil Protection, where Bonaccorso et al. (2005) described on-site responses and integration of delivered TADR data into situation appraisals. In this way, dissemination of sensitive data was controlled, allowing information to flow to the source charged with managing the crisis, thereby allowing communication through a single, relevant voice. This followed the dissemination philosophy given in Figure 10. The communication design was also set up so that the recipient, rather than receiving raw data, received fully-processed data that was immediately useable. This was the guiding philosophy of the system: to work with users to provide products, and develop a system, which fitted the user needs, communication protocols and reporting requirements (McArdell, 2002).

Acronyms used (with reference or URL where appropriate)

ALICE:	Absolutely Local Index of Change of Environment (Pergola et al., 2008; 2009)
ATSR:	Along Track Scanning Radiometer
AQUA:	Part of NASA's A-train satellite series
AVHRR:	Advanced Very High Resolution Radiometer
AVO:	Alaska Volcano Observatory
BIRD:	Bispectral Infra-Red Detection
DN:	Digital Number
DPC	Italian Department of Civil Protection
ESA:	European Space Agency
EUMETSAT:	www.eumetsat.int
GOES:	Geostationary Operational Environmental Satellite
GMS:	Geostationary Meteorological Satellite
HIGP:	Hawaii Institute of Geophysics and Planetology
INGV:	Istituto Nazionale di Geofisica e Vulcanologia
IODC:	Indian Ocean Data Coverage (Meteosat-7)
IR:	InfraRed: 0.7 – 20 μm
METOP:	component of the overall EUMETSAT Polar System
MIR:	Mid-InfraRed: 3.0 – 5.0 μm
MODIS:	Moderate-Resolution Imaging Spectroradiometer
MODTRAN:	MODerate resolution atmospheric TRANSmission
MODVOLC:	HIGP MODIS Thermal Alert System (http://modis.higp.hawaii.edu/)
MSG:	Meteosat Second Generation
MTSAT:	Multifunctional Transport Satellite
NASA:	National Aeronautics and Space Administration
NEODAAS:	Earth Observation Data Acquisition and Analysis Service
NERC:	Natural Environment Research Council
NESDIS:	National Environmental Satellite, Data, & Information Service
NIR:	Near InfraRed: 0.7 – 1.1 μm
NOAA:	National Oceanic and Atmospheric Administration
NTI:	Normalized Thermal Index (Wright et al., 2002)
RST:	Robust Satellite Technique (Pergola et al., 2008; 2009)
SEVIRI:	Spinning Enhanced Visible and InfraRed Imager
SSG:	Scientific Synthesis Group (Betaloso et al., 2009)
UNIFI:	University of Florence
TADR:	Time-Averaged Discharge Rate (Harris et al., 2007)
TERRA:	NASA's "flagship Earth observing satellite" (http://terra.nasa.gov/)

TIR:	Longwave InfraRed: 5.0 – 20 µm
UAF:	University of Alaska, Fairbanks
UK:	United Kingdom
VAST:	Volcanic Anomaly SofTware (Higgins and Harris, 1997)
VISSR:	Visible and Infrared Spin Scan Radiometer
USA (or US):	United States of America

References

Arino, O. and Melinotte, J.M. (1995). Fire index atlas. Earth Observation Quarterly, 50, 11-16.

Barberi, F., Civetta, L., Rosi, M., and Scandone, R. (2009) Chronology of the 2007 eruption of Stromboli and the activity of the Scientific Synthesis Group. Journal of Volcanology and Geothermal Research, 182, 123-130.

Bertolaso, G., De Bernardinis, B., Bosi, V., Cardaci, C., Ciolli, S., Colozza, R., Cristiani, C., Mangione, D., Ricciardi, A., Rosi, M., Scalzo, A. and Soddu, P. (2009). Civil protection preparedness and response to the 2007 eruptive crisis of Stromboli Volcano, Italy. Journal of Volcanology and Geothermal Research, 182, 269-277.

Bonaccorso, S., Calvari, S., and Boschi, E. (2015) Hazard mitigation and crisis management during major flank eruptions at Etna volcano: reporting on real experience. This volume.

Brustet, J.M., Vickos, J.B., Fontain, J., Manissadjan, K., Podaire, A. and Lavenu, F. (1991). Remote sensing of biomass burning in West Africa with NOAA-AVHRR. In Global Biomass Burning: atmospheric, climatic and bisopheric implications, ed J. Levine, MIT Press, pp. 47-52.

Calvari, S. and Pinkerton, H. (1998) Formation of lava tubes and extensive flow field during the 1991-1993 eruption of Mount Etna. J. Geophys. Res., 103(B11), 27291-27301.

Calvari, S., Spampinato, L., Lodato, L., Harris, A.J.L., Patrick, M.R., Dehn, J., Burton, M.R. and Andronico, D. (2005). Chronology and complex volcanic processes during the 2002-2003 flank eruption at Stromboli volcano (Italy) reconstructed from direct observations and surveys with a handheld thermal camera. Journal of Geophysical Research, 110, B02201. DOI: 10.1029/2004JB003129

Calvari, S., Lodato, L., Steffke, A., Cristaldi, A.., Harris, A.J.L., Spampinato, L. and Boschi, E. (2010). The 2007 Stromboli eruption: Event chronology and effusion rates using thermal infrared data. Journal of Geophysical Research, 115, B04201. DOI: 10.1029/2009JB006478.

Chuvieco, E. and Martin, M.P. (1994). A simple method for fire growth mapping using AVHRR channel 3 data. International Journal of Remote Sensing, 15(16), 3141-3146.

Cracknell, A.P. (1997). The Advanced Very High Resolution Radiometer, London: Taylor & Francis, 534 p.

561 Cracknell, A.P. and Hayes, L.W.B. (1991). Introduction to Remote Sensing, London: Taylor & Francis,
562 293 p.

563 Dean, K., Searcy, C., Wyatt, C., George, S. and Engle, K. (1996). Monitoring volcanoes in the North
564 Pacific Ocean region using satellite imagery, modeling and meteorological data. Proceedings of the
565 Pan Pacific Hazards Conference. Vancouver (Canada): 27 July – 4 August, 1996, p. 1-29.

566 Dean, K., Servilla, M., Roach, A., Foster, B. and Engle, K. (1998). Satellite monitoring of remote
567 volcanoes improves study efforts in Alaska. EOS, Transactions, American Geophysical Union, 79(35),
568 413-423.

569 Dehn, J., Dean, K. and Engle, K. (2000). Thermal monitoring of North Pacific volcanoes from space.
570 Geology, 28(8), 755-758.

571 Di Bello, G., Filizzola, C., Lacava, T. Marchese, F., Pergola, N., Pietrapertosa, C., Piscitelli, S., Scaffidi, I.
572 and Tramutoli, V. (2004). Robust satellite techniques for volcanic and hazards monitoring. Annals of
573 Geophysics, 47(1), 49-64.

574 Dozier, J. (1980). Satellite identification of surface radiant temperature fields of subpixel resolution.
575 NOAA Technical Memorandum, NOAA-81021710, Washington DC: National Earth Satellite Service, 17
576 p.

577 Flannigan, M.D. and Vonder Haar, T.H. (1986). Forest fire monitoring using NOAA satellite AVHRR.
578 Canadian Journal of Forest Research, 16, 975-982.

579 Flasse, S.P. and Ceccato, P. (1996). A contextual algorithm for AVHRR fire detection. International
580 Journal of Remote Sensing, 17(2), 419-424.

581 Flynn, L., Wright, R., Garbeil, H., Harris, A. and Pilger, E. (2002). A Global Thermal Alert System Using
582 MODIS: Initial Results from 2000-2001. Advances in Environmental Monitoring and Modeling, 1(3),
583 37-69.

584 Franca, J.R.A., Brustet, J.-M. and Fontan, J. (1995). Multispectral remote sensing of biomass burning
585 in West Africa. Journal of Atmospheric Chemistry, 22, 81-110.

586 Ganci, G., Harris, A.J.L., Del Negro, C., Guehenneux, Y., Cappello, A., Labazuy, P., Calvari, S. and
587 Gouhier, M. (2012). A year of lava fountaining at Etna: Volumes from SEVIRI. Geophysical Research
588 Letters, 39, L06305. DOI: 10.1029/2012GL051026.

589 Groom, S., Land, P., Miller, P., Shutler, J., Smyth, T., Kirby, N., Brooks, A., and Siddorn, J., (2006) The
590 NERC Earth Observation Data Acquisition and Analysis Service (NEODAAS) – a new partnership for
591 supporting the UK academic community. In: Proceedings of the Remote Sensing Society conference
592 Reading, September 2006.

593 Harris, A.J.L. (1992). Volcano detection and monitoring using AVHRR: The Krafla eruption, Iceland,
594 1984. Masters Thesis, Department of Applied Physics and Electronics and Manufacturing Engineering,
595 University of Dundee, 206 p.

596 Harris, A.J.L. (1996). Towards automated fire monitoring from space: semi-automated mapping of
597 the January 1994 New South Wales wild-fires using AVHRR data. International Journal of Wildland
598 Fire, 6(3), 107-116.

599 Harris, A., (2013) Thermal Remote Sensing of Active Volcanoes: A User's Manual. Cambridge
600 University Press, 728 p.

601 Harris, A.J.L. and Thornber, C. (1999). Complex effusive events at Kilauea as documented by the GOES
602 satellite and remote video cameras. Bulletin of Volcanology, 61(6), 382-395.

603 Harris, A.J.L. and Neri, M. (2002). Volumetric observations during paroxysmal eruptions at Mount
604 Etna: pressurized drainage of a shallow chamber or pulsed supply? J. Volcanol. Geotherm. Res., 116,
605 79-95.

606 Harris, A.J.L., and Baloga, S. M. (2009), Lava discharge rates from satellite-measured heat flux.
607 Geophys. Res. Lett., 36, L19302, doi:10.1029/2009GL039717

608 Harris, A.J.L., Swabey, S.E.J. and Higgins, J. (1995a) Automated thresholding of active lavas using
609 AVHRR data. Int. J. Remote Sensing, 16(18), 3681-3686.

610 Harris, A.J.L., Vaughan, R.A. and Rothery, D.A. (1995b) Volcano detection and monitoring using
611 AVHRR data: the Krafla eruption, 1984. Int. J. Remote Sensing, 16(6), 1001-1020.

612 Harris, A.J.L., Rothery, D.A., Carlton, R.W., Langaas, S. and Mannstein, H. (1995c) Non-zero saturation
613 of AVHRR thermal channels over high temperature targets: evidence from volcano data and a
614 possible explanation. Int. J. Remote Sensing, 16(1), 189-196.

615 Harris, A.J.L., Butterworth, A.L., Carlton, R.W., Downey, I., Miller, P., Navarro, P. and Rothery, D.A.
616 (1997a) Low cost volcano surveillance from space: case studies from Etna, Krafla, Cerro Negro, Fogo,
617 Lascar and Erebus. Bull. Volcanol., 59, 49-64.

618 Harris, A.J.L., Blake, S., Rothery, D.A. and Stevens, N.F. (1997b) A chronology of the 1991 to 1993 Etna
619 eruption using AVHRR data: implications for real time thermal volcano monitoring. J. Geophys. Res.,
620 102(B4), 7985-8003.

621 Harris, A.J.L., Keszthelyi, L., Flynn, L.P., Mouginis-Mark, P.J., Thornber, C., Kauahikaua, J., Sherrod, D.,
622 Trusdell, F., Sawyer, M.W. and Flament, P. (1997c). Chronology of the Episode 54 eruption at Kilauea
623 Volcano, Hawaii, from GOES-9 satellite data. Geophysical Research Letters, 24(24), 3281-3284.

624 Harris, A.J.L., Wright, R. and Flynn, L.P. (1999). Remote monitoring of Mount Erebus Volcano,
625 Antarctica, using Polar Orbiters: Progress and Prospects. Internal Journal of Remote Sensing,
626 20(15&16), 3051-3071.

627 Harris, A.J.L., Flynn, L.P., Dean, K., Pilger, E., Wooster, M., Okubo, C., Mouginis-Mark, P., Garbeil, H.,
628 De la Cruz Reyna, S., Thornber, C., Rothery, D. and Wright, R. (2000a). Real-time Monitoring of
629 Volcanic Hot Spots with Satellites. American Geophysical Union Monograph Series, 116, 139-159.

630 Harris, A.J.L., Murray, J.B., Aries, S.E., Davies, M.A., Flynn, L.P., Wooster, M.J., Wright, R. and Rothery,
631 D.A. (2000b). Effusion rate trends at Etna and Krafla and their implications for eruptive mechanisms.
632 Journal of Volcanology and Geothermal Research, 102(3-4), 237-269.

633 Harris, A.J.L., Pilger, E., Flynn, L.P., Garbeil, H., Mouginis-Mark, P.J., Kauahikaua, J. and Thornber, C.
634 (2001). Automated, high temporal resolution, thermal analysis of Kilauea volcano, Hawaii, using
635 GOES-9 satellite data. International Journal of Remote Sensing, 22(6), 945-967.

636 Harris, A.J.L., Pilger, E., and Flynn, L.P. (2002a) Web-based hot spot monitoring using GOES: what it is
637 and how it works. Advances in Environmental Monitoring and Modeling, (http://www.kcl.ac.uk/ kis/
638 schools/ hums/ geog/ advemm/ vol1no3.html) 1(3), 5-36.

639 Harris, A.J.L., Pilger, E., Flynn, L.P. and Rowland, S.K. (2002b) Real-Time Hot Spot Monitoring using
640 GOES: Case Studies from 1997-2000. Advances in Environmental Monitoring and Modeling, 1(3), 134-
641 151.

642 Harris, A.J.L., Dehn, J., and Patrick, M. (2003) Calculation of Lava Effusion Rates at Stromboli Volcano
643 using FLIR Data. DPC Contractor Report, COA (Stromboli), 16 June 2003, 15 p.

644 Harris, A.J.L., Dehn, J., Patrick, M., Calvari, S., Ripepe, M. and Lodato, L. (2005). Lava Effusion Rates
645 from Hand-Held Thermal Infrared Imagery: An Example from the June 2003 Effusive Activity at
646 Stromboli. Bulletin of Volcanology, 68, 107-117.

647 Harris, A.J.L., Dehn, J., and Calvari, S., 2007, Lava Effusion Rate Definition and Measurement: A
648 Review, Bull. Volcanol., 70:1–22, DOI 10.1007/s00445-007-0120-y.

649 Harris, A.J.L., Favalli, M., Steffke, A., Fornaciai, A. and Boschi, E. (2010). A relation between lava
650 discharge rate, thermal insulation, and flow area set using lidar data. Geophysical Research. Letters,
651 37, L20308. DOI: 10.1029/2010GL044683.

652 Harris, A., Steffke, A., Calvari, S., and Spampinato, L. (2011) Thirty years of satellite-derived lava
653 discharge rates at Etna: Implications for steady volumetric output. J. Geophys. Res., Vol. 116, No. B8,
654 B08204 http://dx.doi.org/10.1029/2011JB008237.

655 Harris et al. (2015) Conclusion: Recommendations and findings of the RED SEED working group. This
656 Volume

657 Higgins, J. and Harris, A.J.L. (1997) VAST: a program to locate and analyse volcanic thermal anomalies
658 automatically from remotely sensed data. Computers and Geosciences, 23(6), 627-645.

659 ISTAT (2008) Demografia in cifre. Istituto Nazionale di Statistica, Roma, Italy. http://demo.istat.it/.

660 Justice, C. and Dowty, P. (1994). IGBP-DIS Satellite Fire Detection Algorithm Workshop Technical
661 Report. International Geosphere Biosphere Programme Working Paper, 9, Workshop held at
662 NASA/GSFC, Greenbelt (MA), 25-26 February 1997, 88 p.

663 Kaufman, Y.J., Setzer, A., Justice, C., Tucker, C.J., Pereira, M.C. and Fung, I. (1990). Remote Sensing of
664 biomass burning in the tropics. In Fire in the tropical biota, ed J. Goldhammer, Berlin: Springer-
665 Verlag, pp. 371-399.

666 Kaufman, Y.J., Kleidman, R.G. and King, M.D. (1998). SCAR-B fires in the tropics: Properties and
667 remote sensing from EOS-MODIS. Journal of Geophysical Research, 103(D24), 31,955-31,968

668 Kennedy, P.J., Belward, A.S. and Grégoire, J.-M. (1994). An improved approach to fire monitoring in
669 West Africa using AVHRR data. International Journal of Remote Sensing, 15(11), 2235-2255.

670 Kidwell, K.B. (1998) NOAA Polar Orbiter Data User's Guide, U.S. Department of Commerce, National
671 Oceanic and Atmospheric Administration, National Environmental Satellite, Data, and Information
672 Service, http://www.ncdc.noaa.gov/oa/pod-guide/ncdc/docs/podug/index.htm.

673 Langaas, S. (1993). A parametrised bispectral model for savanna fire detection using AVHRR night
674 images. International Journal of Remote Sensing, 14(12), 2245-2262.

675 Lee, T.F. and Tag, P.M. (1990). Improved detection of hotspots using the AVHRR 3.7 μm channel.
676 American Meteorological Society, 71(12), 1722-1730.

677 Lodato, L., Spampinato, L., Harris, A., Calvari, S., Dehn, J., and Patrick, M., 2007, The Morphology and
678 Evolution of the Stromboli 2002-03 Lava Flow Field: An Example of Basaltic Flow Field Emplaced on a
679 Steep Slope, Bull. Volcanol., 69, 661-679

680 Matson, M. and Dozier, J. (1981). Identification of subresolution high temperature sources using a
681 thermal IR sensor. Photogrammetric Engineering and Remote Sensing, 47(9), 1311-1318.

682 McArdell, L. (2002) A review of the effectiveness of a web site for communicating hot spot
683 information. Masters dissertation, The Open University (UK), 59 p + Appendices.

684 Miller, P., Groom, S., Mcmanus, A., Selley, J. and Mironnet, N. (1997) PANORAMA: a semi-automated
685 AVHRR and CZCS system for observation of coastal and ocean processes. RSS97: Observations and
686 Interactions, In: Proceedings of the Remote Sensing Society conference Reading, September 1997,
687 539-544.

688 Moxey, L., Harris, A., Patrick, M., Calvari, S., and Evans-Jones, K. (2003) Satellite-based hazard
689 monitoring and prediction: a case study from Mt. Etna. Cities on Volcanoes III, Hilo, Hawaii, July 14-
690 18, 2003

691 Muirhead, K., and Cracknell, A.P. (1984) Identification of gas flares in the North Sea using satellite
692 data. International Journal of Remote Sensing, 5, 199-212.

693 Muirhead, K., and Cracknell, A.P. (1985) Straw burning over Great Britain detected by AVHRR.
694 International Journal of Remote Sensing, 6, 827-833.

695 NOAA NESDIS (2015a) Comprehensive large array-data stewardship system. NOAA Satellite
696 Information Service, National Environmental Satellite, Data, and Information Service,
697 http://www.nsof.class.noaa.gov/data_available/avhrr/index.htm, downloaded 2 April 2015.

698 NOAA NESDIS (2015b) About NESDIS, National Environmental Satellite, Data, and Information
699 Service, http://www.nesdis.noaa.gov/about_nesdis.html, downloaded 2 April 2015.

700 Pergola, N., Pietrapertosa, C., Lacava, T. and Tramutoli, V. (2001). Robust satellite techniques for
701 monitoring volcanic eruptions. Annali di Geofisica, 44(2), 167-177.

702 Pergola, N., Marchese, F., Tramutoli, V., Filizzola, C. and Ciampa, M. (2008). Advanced satellite
703 technique for volcanic activity monitoring and early warning. Annals of Geophysics, 51(1), 287-301.

Pereira, M.C. and Setzer, A.W. (1993). Spectral characteristics of deforestation fires in NOAA/AVHRR images. International Journal of Remote Sensing, 14(3), 583-597.

Pergola, N., D'Angelo, G., Lisi, M., Marchese, F., Mazzeo, G. and Tramutoli, V. (2009). Time domain analysis of robust satellite techniques (RST) for near real-time monitoring of active volcanoes and thermal precursor identification. Physics and Chemistry of the Earth, 34, 380-385.

Prins, E.M. and Menzel, W.P. (1994). Trends in South American biomass burning detected with the GOES visible infrared spin scan radiometer atmospheric sounder from 1983-1991. Journal of Geophysical Research, 99(D8), 16,719-16,735.

Robel, J. (2009) NOAA KLM user's guide with NOAA-N, -N' supplement, U.S. Department of Commerce, National Oceanic and Atmospheric Administration, National Environmental Satellite, Data, and Information Service, http://www.ncdc.noaa.gov/oa/pod-guide/ncdc/docs/klm/cover.htm.

Roberts, G.J., and Wooster, M.J. (2008) Fire Detection and Fire Characterization Over Africa Using Meteosat SEVIRI. Geoscience and Remote Sensing, IEEE Transactions on Geoscience and Remote Sensing 46(4): 1200 – 1218.

Robinson, J.M. (1991) Fire from space: Global fire evaluation using infrared remote sensing. International Journal of Remote Sensing, 12(1): 3-24.

Setzer, A.W. and Pereira, M.C. (1991). Amazonia biomass burnings in 1987 and an estimate of their tropospheric emissions. Ambio, 20(1), 19-22.

Setzer, A.W. and Verstraete, M.M. (1994). Fire and glint in AVHRR's channel 3: a possible reason for the non-saturation mystery. International Journal of Remote Sensing, 15(3), 711-718.

Shutler, J.D., Smyth, T.J. Land, P.E. and Groom, S.B. (2005). A near real-time automatic MODIS data processing system. International Journal of Remote Sensing, 25 (5), 1049-1055.

Steffke, A.M. and Harris, A.J.L. (2011). A review of algorithms for detecting volcanic hot spots in satellite infrared data. Bulletin of Volcanology, 73, 1109-1137.

Stevens, N.F., Murray, J.B., Wadge, G. (1997). The volume and shape of the 1991–1993 lava flow field at Mount Etna, Sicily. Bull Volcanol, 58, 449-454.

Taddeucci, J., Pompilio, M., and Scarlato, P. (2002) Monitoring the explosive activity of the July-August 2001 eruption of Mt. Etna (Italy) by ash characterization, Geophysical Research Letters, 29, 1029-1032.

733 Taddeucci J., Pompilio, M., and Scarlato, P. (2004) Conduit processes during the July-August 2001
734 explosive activity of Mt. Etna (Italy): inferences from glass chemistry and crystal size distribution of
735 ash particles, Journal of Volcanology and Geothermal Research, 137, 33-54.

736 Tramutoli, V. (1998). Robust AVHRR Techniques (RAT) for environmental monitoring: theory and
737 applications. Proceedings of SPIE, 3496, 101-113.

738 Tramutoli,V., Di Bello, G., Pergola, N. and Piscitelli, S. (2001). Robust satellite techniques for remote
739 sensing of seismically active areas. Annali di Geofisica, 44(2), 295-311.

740 Vermote, E., Ellicott, E., Dubovik, O., Lapyonok, T., Chin, M., Giglio, L., and Roberts, G.J. (2009) An
741 approach to estimate global biomass burning emissions of organic and black carbon from MODIS fire
742 radiative power, Journal of Geophysical Research, 114, D18205, DOI: 10.1029/2008JD011188.

743 Vicari, A., Ciraudo, A., Del Negro, C., Herault, A., Fortuna, L. (2009). Lava flow simulations using
744 discharge rates from thermal infrared satellite imagery during the 2006 Etna eruption. Natural
745 Hazards, 50, 539–550, doi: 10.1007/s11069-008-9306-7.

746 Vicari, A., Bilotta, G., Bonfiglio, S., Cappello, A., Ganci, G., Hérault, A., Rustico, E., Gallo, G., Del Negro,
747 C. (2011). LAV@HAZARD: A web-GIS interface for volcanic hazard assessment. Annals of Geophysics,
748 54, 5, doi: 10.4401/ag-5347;

749 Wooster, M.J., Zhukov, B. and Oertel, D. (2003). Fir radiative energy for quantitative study of biomass
750 burning: derivation from the BIRD experimental satellite and comparison to MODIS fire products.
751 Remote Sensing of Environment, 86, 83-107.

752 Wright, R., Blake, S., Harris, A., and Rothery, D. (2001). A simple explanation for the space-based
753 calculation of lava eruptions rates, Earth and Planetary Science Letters, 192, 223-233.

754 Wright, R., Flynn, L., Garbeil, H., Harris, A. and Pilger, E. (2002). Automated volcanic eruption
755 detection using MODIS. *Remote Sensing of Environment*, **82**, 135-155.

756 Wright, R., Flynn, L.P., Garbeil, H., Harris, A.J.L. and Pilger, E. (2004). MODVOLC: near-real-time
757 thermal monitoring of global volcanism. Journal of Volcanology and Geothermal Research, 135, 29-
758 49.

759

Figure Captions

Figure 1. (a) coverage of the NEODAAS-Dundee station, and (b) frequency of pass by geographical position within the mask.

Figure 2. NEODAAS-Plymouth hot spot browser for Etna and Stromboli. The example is from 10 March 2013, and hot spots are apparent at Mt. Etna's summit due to effusive and fountaining activity at the SE Crater. In this single-band black-and white rendition, black is cold and white is hot.

Figure 3. (a) AVHRR channel 4 sub-image of Sicily and Calabria obtained at 00:46Z on 29 May 2001. Sub-image is 320 × 300 pixels, or ~350 × 330 km, in size. Lighter tones indicate higher pixel-integrated spectral radiances. The Aeolian islands of Alicudi, Filicudi, Salina, Lipari, Vulcano, Panarea and Stromboli are labeled using the first letter of each islands name. The oil refinery at, and cape of, Milazzo are located using the red circle (the oil refinery registers a hot spot in the AVHRR MIR and TIR bands). Yellow circle contains an "apparent" hot spot due to the presence of a lake (Biviere di Lentini) which appears relatively warm by night (against the cool land background) and relatively cool by day (against the warm, solar-heated, land background). Note that the real hot spot on Etna is somewhat crisper (more cleanly defined) than the fuzzier "apparent" hot spot of the lake, and two other lake-related "apparent" hot spots can be seen to the SW of Etna. Mount Etna is located using the red box, and is magnified top right. In this nighttime image, the sea (like the lake) is relatively warm (lighter tones) compared with the land (darker tones), and Etna is apparent as a cold, circular, feature (due to its elevation, surface temperatures decrease with height causing the volcano to appear as a cold zone). The hot spot at Etna's summit is centered in the yellow box and magnified lower right. The hot spot is due to pixels containing active lava, and is obvious as a group of hot (white) pixels against a cold (black) background. (b) AVHRR channel 4 sub-image of Sicily and Calabria obtained at 00:36Z on 30 May 2001 (from Electronic Supplement 7 of Harris, 2013).

Figure 4. Schematic summarizing implementation of the VAST hot spot detection algorithm (from Higgins and Harris (1997, Fig. 3): with permission from Elsevier). The algorithm used three equations a executes five steps.

Figure 5. Pixel grids of AVHRR channel 4 brightness temperature centered on Mt. Etna's summit hot spot for (a) the 29 May, and (b) the 30 May 2001 sub-images of Figure 3. Values are brightness temperature plus 30 °C multiplied by 100. Area of the anomaly is marked by the red line, with a potential extra "anomalous" pixel in the 30 May being highlighted in yellow. Inclusion of this pixel increases the TADR estimate from 1.7 – 2.1 $m^3 s^{-1}$ to 2.0 – 2.3 $m^3 s^{-1}$ (from Electronic Supplement 7 of Harris, 2013).

792 **Figure 6.** Pixel grids of AVHRR channel 4 brightness temperature centered on Mt. Etna's summit hot
793 spot for (a) the 29 May, and (b) the 30 May 2001 sub-images of Figure 3. Values defined within the
794 hot spot are given in red, and "cold" background pixels are given in blue; these are linked to the
795 "hot" pixels for which they are used to characterize the background spectral radiance in the mixture
796 model using the blue, arrowed, line (from Electronic Supplement 7 of Harris, 2013).

797 **Figure 7.** AVHRR quick look products for (a) the Mt. Etna tile and (b) the Iceland tile; with (c) AVHRR
798 quick look during eruptive activity at Mt Etna in 2001 (AVHRR channel 4 brightness temperature, 22
799 July 2001 15:48 GMT) and (d) MODIS quick look during eruptive activity during 2002 (MODIS top-of-
800 atmosphere true-colour, 28 Oct. 2002 12:15 GMT).

801 **Figure 8.** TADR checks completed during Etna's 2001 eruption. Field observations were provided by
802 Sonia Calvari (INGV-CT) based on channel dimensions and lava flow velocity upon derivation, field
803 mapping estimates were based on the change in volume of the flow field over 24 hour increments.
804 Lines simply link data points and may not be representative of the actual trend between each linked-
805 point.

806 **Figure 9.** AVHRR channel 4 image of 24 July 2001 (00:58 GMT) showing two hot spots cut by a (cold)
807 plume due to phreatomagmatic activity (Taddeucci et al., 2002; 2004) at the Piano del Lago cone at
808 2500 m (dark is cold; bright is hot). The northern hot spot is due to lava flows from fissures in the
809 summit zone; southern hot spot is due the active lava flow (LSF1) advancing towards Nicolosi and
810 Belpasso. (a) Georeferenced channel 4 image, and (b) fitted to a town and road grid. In addition, the
811 best images were fitted to a DEM of Etna (c). Fit given in (c) is the image for 25 July 2001 at 00:54
812 GMT.

813 **Figure 10.** Response model and flow of data/information through the hot spot response system
814 implemented at HIGP. Example agencies are given on the basis of the Etna 2001 and 2002, as well as
815 the Stromboli 2002-2003 and 2007, experiences. A qualitative assessment of the time delay for data
816 or information provision is indicated at each step. Dashed line is a communication "wall", where we
817 link into the base of the local communication protocol, where the local communication protocol
818 linked to here is a crude summary of that detailed by Bertolaso et al. (2009) for Stromboli's 2007
819 effusive crisis.

820

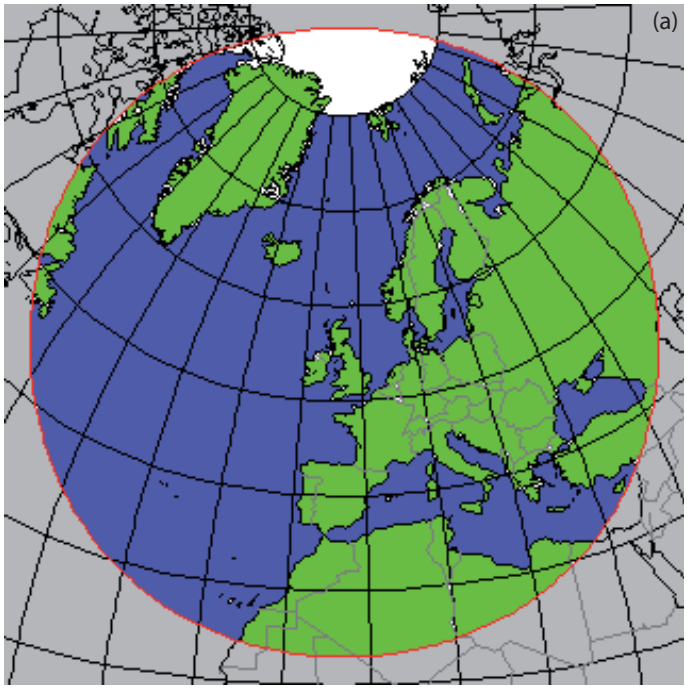

coverage from Dundee (b)

image frequency

low high

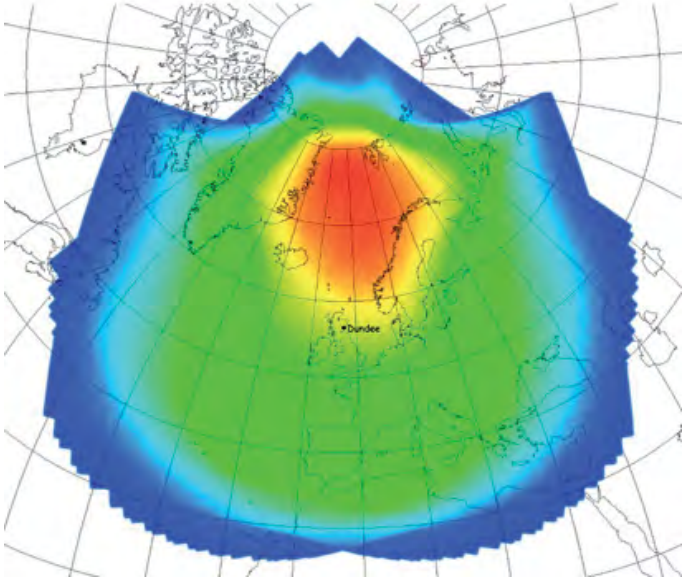

AVHRR 1km

Brightness Temperature 3

Sunday, 10 March 2013

Mission lifetime:
19/Nov/1978 to present

Brightness Temperature 3 image nearest to 10th Mar 2013	This week's Brightness Temperature 3		Brightness Temperature 3 Composite
10th Mar 2013 11:49 (99% valid pixels)	9th Mar 2013 00:23 (99% valid pixels)	8th Mar 2013 00:34 (99% valid pixels)	There are no composites for this area
	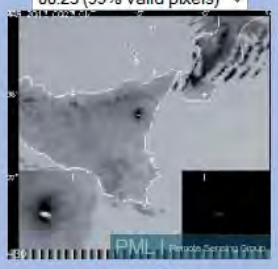	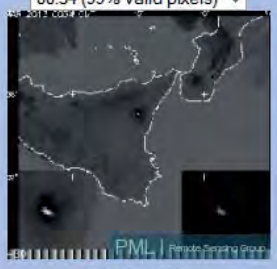	
You are viewing scenes: Switch to Composites	7th Mar 2013 12:21 (99% valid pixels)	6th Mar 2013 12:32 (99% valid pixels)	
	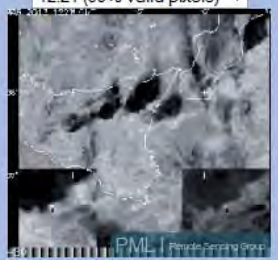	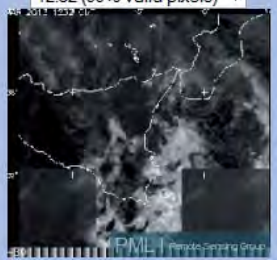	

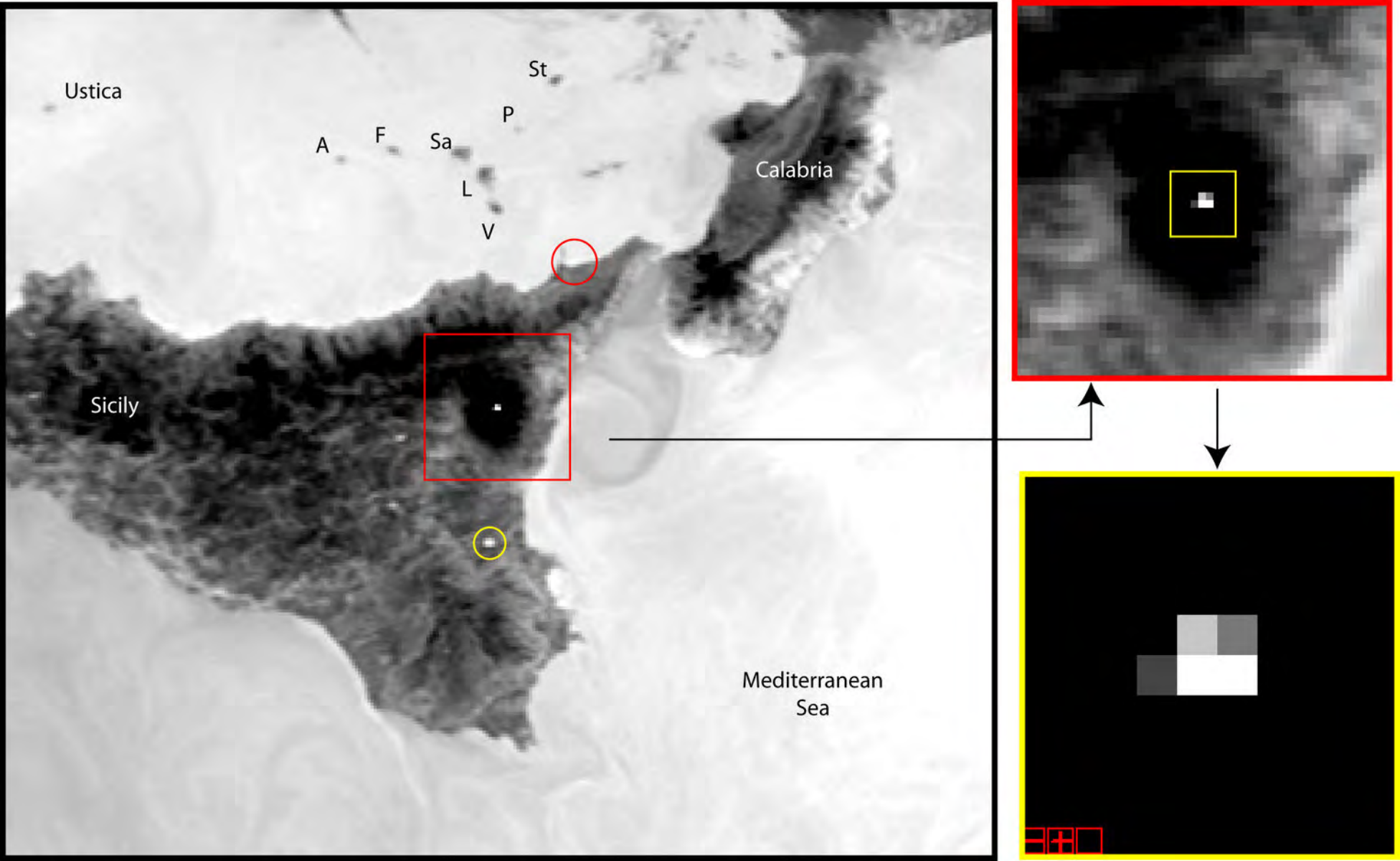
Ustica
St
P
A
F
Sa
L
V
Calabria
Sicily
Mediterranean
Sea

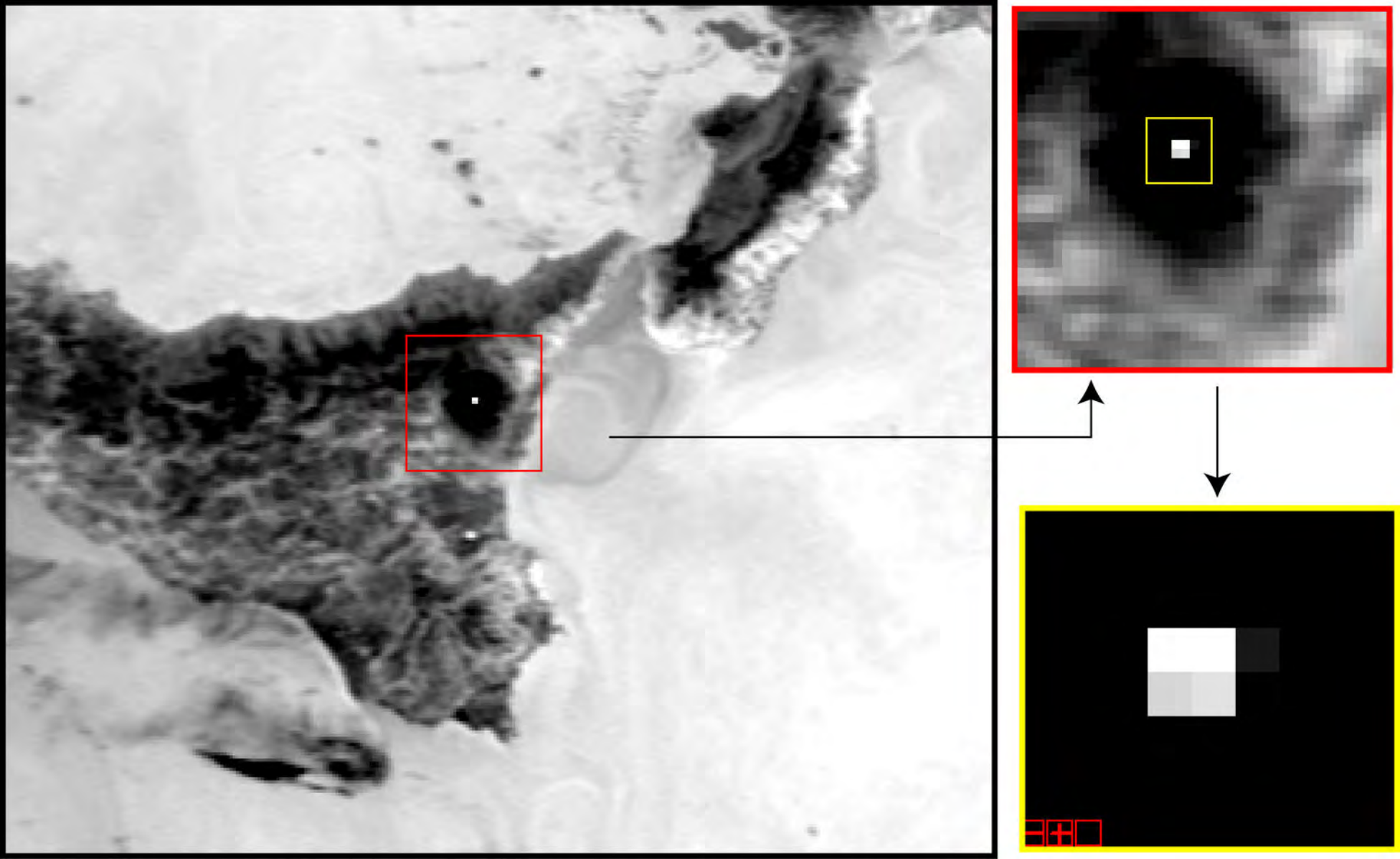

(A) ALGORITHM STEPS

Step 1

Create ΔT image (= pixel area within the black box).

Step 2

Define volcano sub-image (= all pixels within the grey box).

Step 3

Apply equations A & B to all pixels in the non-volcanic zone (= all pixels within the black box but outside the grey box) on a pixel by pixel basis. Store the maximum ΔT_{diff}. Natural variation (ΔT_{nat}) is set equal to maximum ΔT_{diff}

Step 4

Apply equations A, B & C to all pixels in the volcano sub-image on a pixel by pixel basis.

Step 5

Iterate step 4, excluding pixels flagged as "hot" in a previous iteration from equation A, until no new "hot" pixels are found.

(B) ΔT IMAGE

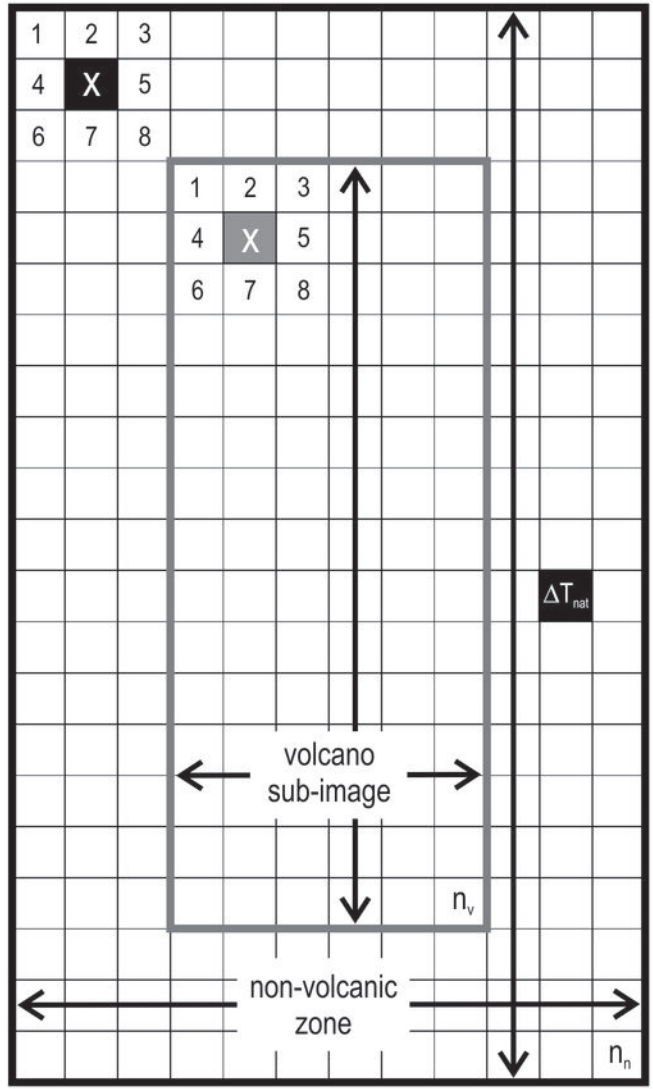

n_n = number of pixels in the non-volcanic zone
n_v = number of pixels in the volcanic sub-image

(C) EQUATIONS

Equation A

$$\Delta T_{neigh} = \frac{\sum_{i=1}^{8} \Delta T_i}{8}$$

in which $\Delta T_i = \Delta T$ for neighbourhood pixel i, where i = 1 to 8

Equation B

$\Delta T_{diff} = \Delta T_x - \Delta T_{neigh}$
in which $\Delta T_x = \Delta T$ for pixel x

Equation C

If $\Delta T_{diff} > \Delta T_{nat}$
then pixel is "hot"
else pixel is "cold"

KEY

X — Current target pixel in the non-volcanic zone with temperature ΔT_i, where i = 1 to n_n

ΔT_{nat} — Non-volcanic zone pixel with maximum ΔT_{diff} (= ΔT_{nat})

X — Current target pixel in the volcano sub-image with temperature ΔT_i, where i = 1 to n_v

(a) 29 May 2001, 0046Z

30 85	27 45	23 40	24 38	28 64
30 05	33 50	46 82	43 81	32 40
32 24	41 80	60 31	53 73	34 32
29 95	31 52	35 29	33 14	30 26

(b) 30 May 2001, 0036Z

32 77	33 20	32 14	31 74	32 40
40 64	49 22	49 36	42 06	36 27
40 56	47 62	47 90	41 41	36 67
29 52	28 09	29 24	32 79	34 87

(a) 29 May 2001, 0046Z

30 85	27 45	23 40	24 38	28 64
30 05	33 50	46 82	43 81	32 40
32 24	41 80	60 31	53 73	34 32
29 92	31 52	35 29	33 14	30 26

(b) 30 May 2001, 0036Z

32 77	33 20	32 14	31 74	32 40
40 64	49 22	49 36	42 06	36 27
40 56	47 62	47 90	41 41	36 67
29 52	28 09	29 24	32 79	34 87

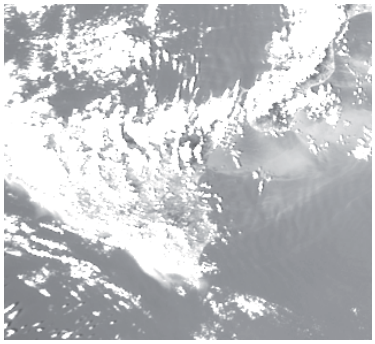

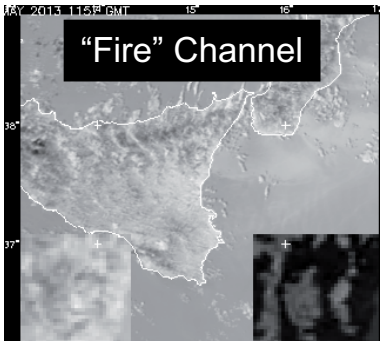

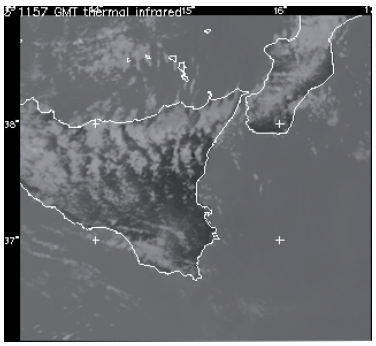

(a) Visible Band (Ch. 1) Mid-infrared Band (Ch. 3) Thermal Band (Ch. 4)

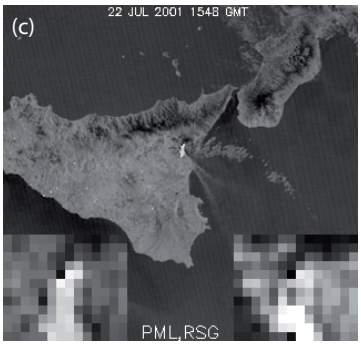

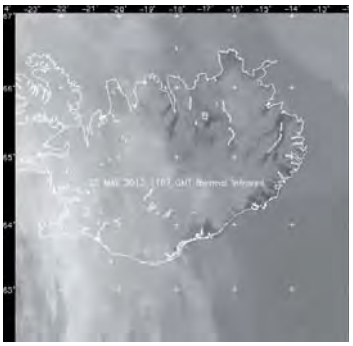

(b) Mid-infrared Band (Ch. 3) Thermal Band (Ch. 4)

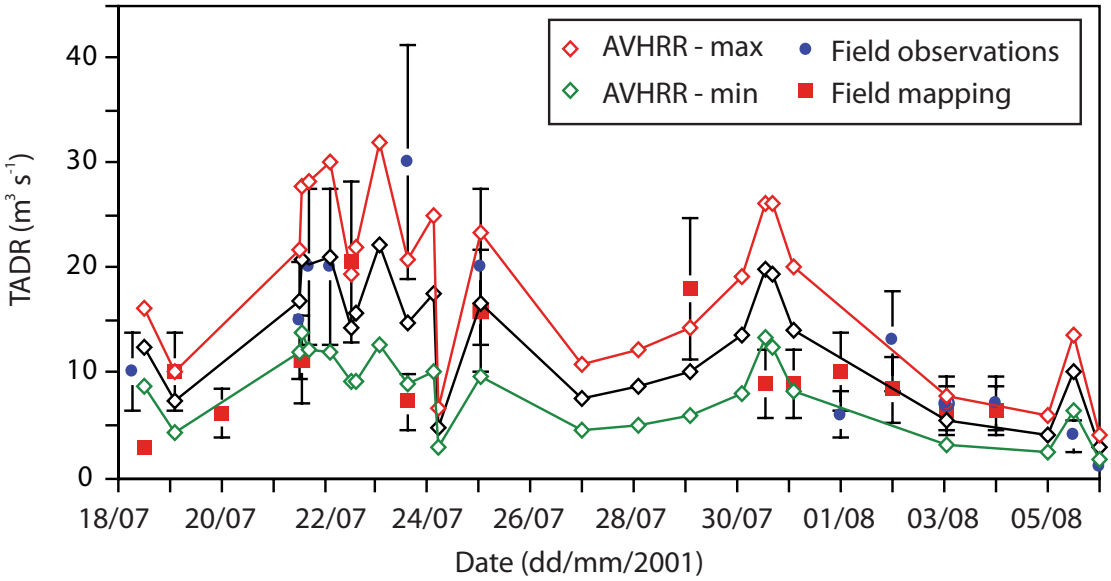
AVHRR - max
AVHRR - min
Field observations
Field mapping
TADR (m3 s-1)
0
10
20
30
40
18/07
20/07
22/07
24/07
26/07
28/07
30/07
01/08
03/08
05/08
Date (dd/mm/2001)

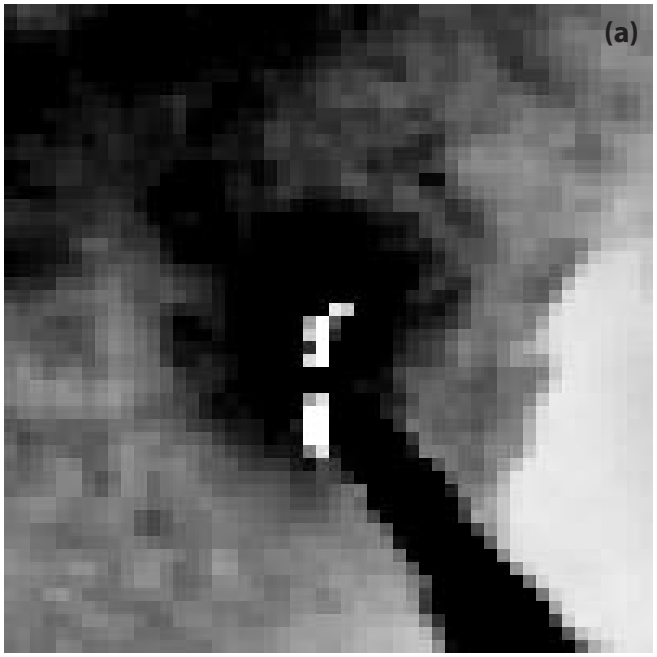
(a)

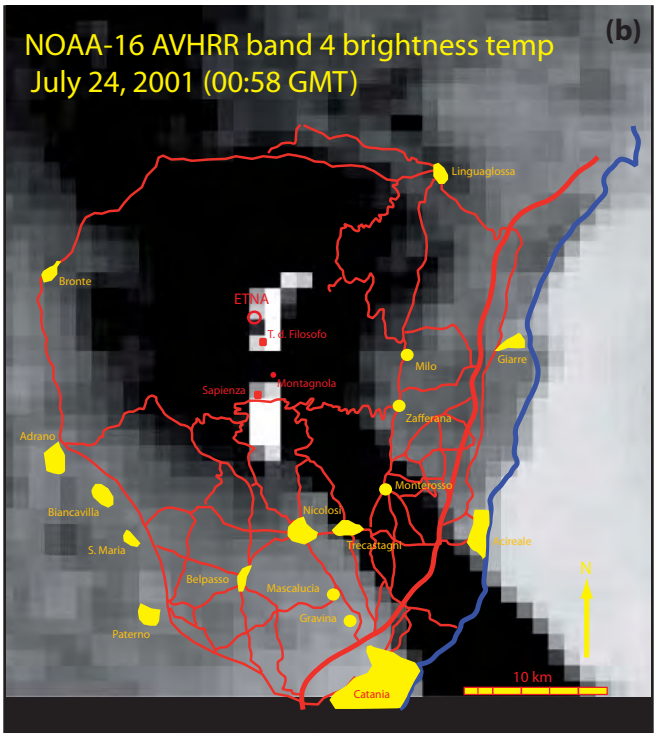
(b)
NOAA-16 AVHRR band 4 brightness temp
July 24, 2001 (00:58 GMT)
Linguaglossa
Bronte
ETNA
T. del Filosofo
Milo
Giarre
Sapienza
Montagnola
Zafferana
Adrano
Monterosso
Biancavilla
Nicolosi
S. Maria
Trecastagni
Acireale
Belpasso
Mascalucia
Gravina
Paterno
Catania
N
10 km

(c)

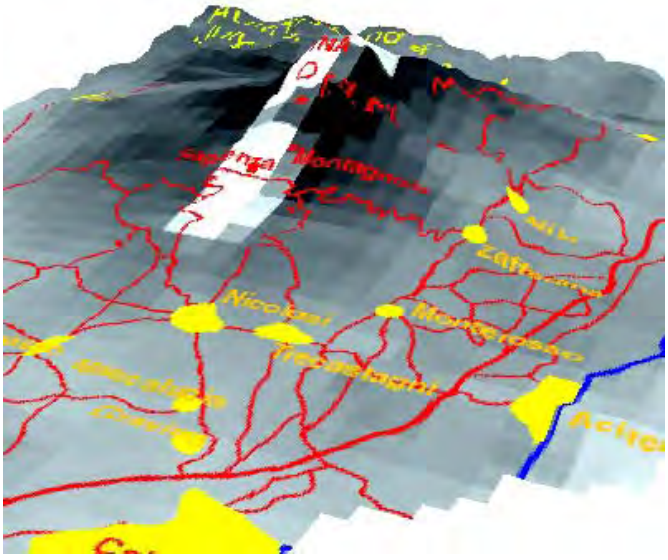

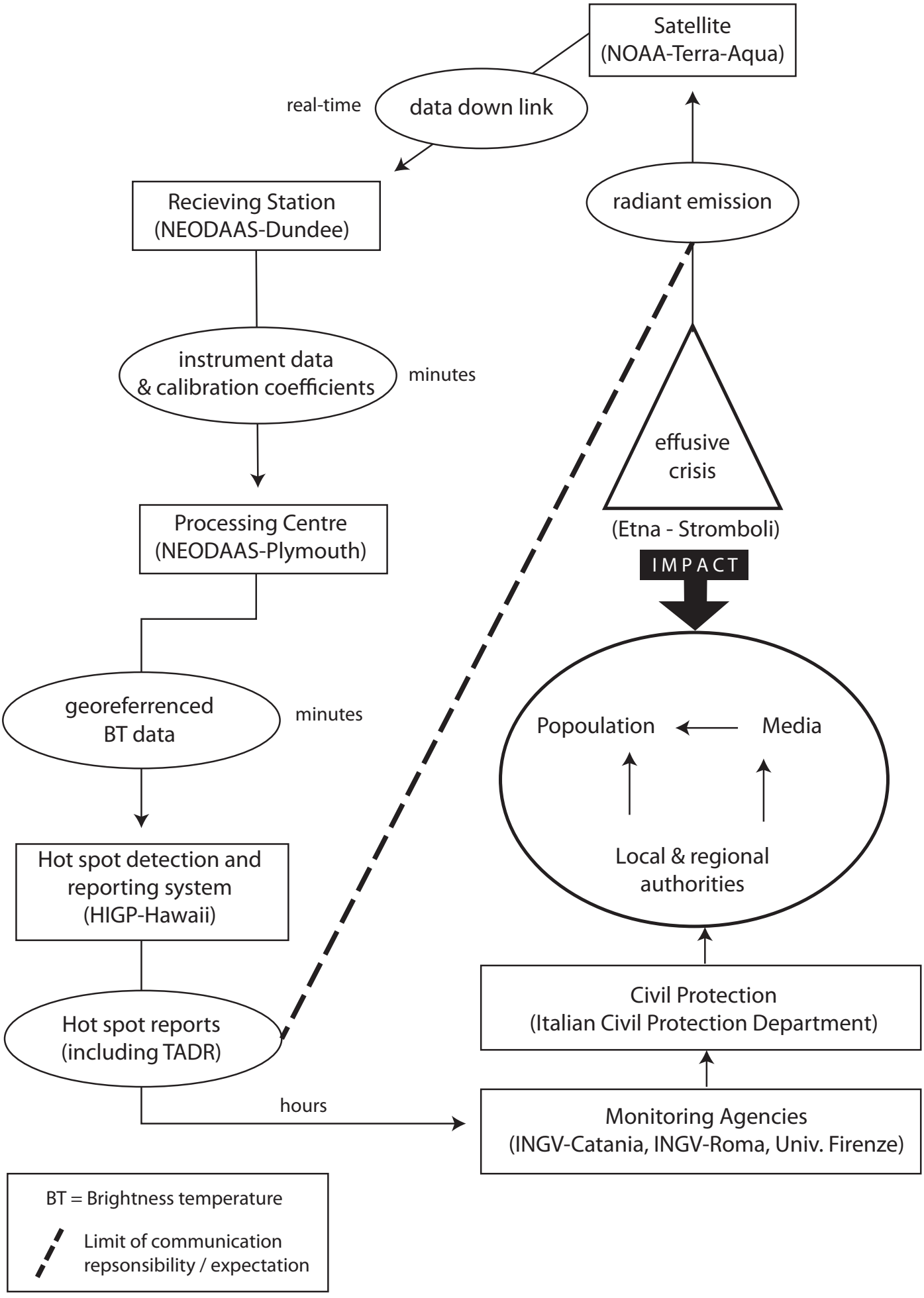
Satellite
(NOAA-Terra-Aqua)
real-time
data down link
Recieving Station
(NEODAAS-Dundee)
radiant emission
instrument data
& calibration coefficients
minutes
effusive
crisis
(Etna - Stromboli)
Processing Centre
(NEODAAS-Plymouth)
IMPACT
georeferrenced
BT data
minutes
Popoulation
Media
Local & regional
authorities
Hot spot detection and
reporting system
(HIGP-Hawaii)
Civil Protection
(Italian Civil Protection Department)
Hot spot reports
(including TADR)
hours
Monitoring Agencies
(INGV-Catania, INGV-Roma, Univ. Firenze)
BT = Brightness temperature
Limit of communication
repsonsibility / expectation

Table 1. Studies, and brief details, of AVHRR studies of fire as reviewed by Robinson (1991) [modified from Table 4 of Robinson (1991)].

Study	Details	Reference
Dozier (1980)	Specifications of algorithms to estimate the size and temperature of sub-pixel hot spots using two bands of infrared (AVHRR) data (i.e., definition of the "dual-band method"). Atmospheric correction methods also considered.	*NOAA Technical Memorandum*, **NOAA-81021710**, Washington, DC
Dozier (1981)	*Ditto*	*Remote Sensing of Environment*, **11**, 221-229.
Matson & Dozier (1981)	The Dozier (1980; 1981) algorithm applied to subpixel hot spots associated with oil flares in the Persian Gulf. Industrial hot spots around Detroit identified.	*Photogrammetric Engineering & Remote Sensing*, **47**, 1311-1318.
Wan (1985)	Simulation of smoke interference with fire signal reception using multiple scattering radiative transfer model linked to model of AVHRR response.	*PhD Dissertation*, University of Santa Barbara (CA).
Matson et al. (1984)	Case study of LAC fire imagery described for various sites; fire sightings in western U.S. compared to hot spots appearing in nighttime (2 am) HRPT images	*NOAA Technical Report*, **NESDIS 7**, Washington, DC.
Muirhead & Cracknell (1984)	Rectification accuracy tested by comparing hot spot locations on rectified LAC (MIR) images containing gas flare locations of known location and associated with North Sea drilling rigs.	*International Journal of Remote Sensing*, **5**, 199-212.
Muirhead & Cracknell (1985)	Hot spots counted on three rectified LAC MIR images of U.K. to assess straw burning and extent of compliance with bans on burning on certain days.	*International Journal of Remote Sensing*, **6**, 827-833.
Malingreau et al. (1985)	Hot spot chronology and NDVI studied of Borneo and East Kalimantan during immense fires of 1983.	*Ambio*, 14, 314-315.
Malingreau (1984)	*Ditto*	*8th International Symposium on Remote Sensing of Environment*, held in Paris (France), 1-4 October 1984. Ann Arbor: Environmental Research Institute of Michigan.
Flannigan (1985)	Fire reports from severe fire outbreak in Alberta compared to fires detected by AVHRR. Dual-band algorithm used to estimate fire size and temperature. Cloud screening applied to reject cloud contaminated pixels	*MSc. Thesis*, Colorado State University, Fort Collins (Colorado).
Flannigan & Vonder Haar (1986)	*Ditto*	*Canadian Journal of Forest Research*, **16**, 975-982.

Matson & Holben (1987)	Hot spots and vegetation studied on one LAC image for a 3×6 ° box over Manaus, Brazil. Dual-band algorithm applied.	*International Journal of Remote Sensing*, **8**, 509-516.
Malingreau & Tucker (1987)	Fire points in Southern Amazon Basin studied on a daily basis over two years in conjunction with studies of NDVI. Inference drawn about penetration of settlement into remote areas.	*Proceedings of IGARSS '87* held in Ann Arbor, Michigan, 18-21 May 1987. IEEE 87CH2434-9 (New York: IEEE), pp. 484-489.
Pereira (1988)	Fire counts and analysis of smoke trajectories with estimates of areas burned and mass combusted based on Brazilian HRPT data of Amazonia. Landsat TM compared to AVHRR.	INPE-4503-tdl/325, Inst. Nactional de Pesquisas Espacias, 12.201 Sao Jose dos Campos, SP, Brazil.
Setzer et al. (1988)	*Ditto*	INPE-4534-RPE/565, Inst. Nactional de Pesquisas Espacias, 12.201 Sao Jose dos Campos, SP, Brazil.

Acronyms:
HRPT: High Resolution Picture Transmission (direct read-out of AVHRR data to ground stations).
GAC: Global Area Coverage.
LAC: Local Area Coverage.
NDVI: Normalized Difference Vegetation Index
[see Cracknell (1997) for full definition of each]

Table 2 Automated fire detection algorithms published in the peer-reviewed literature between 1985 and 1996. Algorithms are listed in chronological order of publication [modified from Harris (2014)]. For more background on algorithm heritage, detail on test set up and execution for each case, see Electronic Supplement 8 of Harris (2013)[§].

Study	Algorithm Type	Tests Executed	Data Type (Application Region)
Flannigan & Vonder Haar (1986)	Contextual	ESTIMATE the mean T_{MIR} and T_{TIR} for cloud-free background pixels from the eight pixels in a 9 × 9 pixel box centered on the target pixel, then: $T_{MIR-t} > \text{mean } T_{MIR-b}$ $T_{TIR-t} > \text{mean } T_{TIR-b}$ $\Delta T > 8$ K (nighttime); $\Delta T > 10$ K (daytime)	AVHRR (Forest fires – Canada)
Kaufman et al. (1990)[(1)]	Fixed (Generic)	$T_{MIR} = 316$ K $\Delta T > 10$ K $T_{TIR} > 250$ K (cloud test)	AVHRR (Fires – Brazil)
Lee and Tag (1990)	Contextual	$T_{TIR} < 263$ K (cloud test) Then; ESTIMATE T_{TIR-b} using the mean of the four side pixels in a 9 × 9 pixel box centered on the target pixel; SELECT a threshold hot component (fire) temperature (T_{fire}) for a two component mixture model and use this, with T_b, to estimate the size of the fire required to yield T_{TIR-t}; USE T_{fire}, T_{TIR-b} and fire size to estimate the corresponding pixel-integrated temperature in the MIR (T_{thresh}) $T_{MIR} < T_{thresh}$	AVHRR (Wild fires – Yellowstone) (Gas flares – Persian Gulf) (Structure fires – California)
Setzer and Pereira (1991)[(2)]	Fixed (Generic)	$T_{MIR} > 319$ K PLUS: manual detection of smoke	AVHRR (Fires – Brazil)
Brustet et al. (1991)	Fixed (Specific)	MIR and TIR thresholds set manually on a case-by-case basis using frequency distributions and T_{TIR} versus T_{MIR} scatter plots.	AVHRR (Wild fires – West Africa)
Kennedy et al. (1994)	Fixed (Generic)	$T_{MIR} > 320$ K $\Delta T > 15$ K $T_{TIR} > 250$ K (cloud test) and/or $R_{NIR} < 16$ % (cloud test)	AVHRR (Wild fires – West Africa)
Langaas (1993)	Contextual	Create frequency distribution of DN_{MIR}; DN_{MIR} with frequency of 50 = DN_{thresh} IF $DN < DN_{thresh}$ AND $T_{fire}^{*} > 470$ K THEN	AVHRR (Wild fires – West Africa)

		pixel is anomalous	
Chuvieco and Martin (1994)	Fixed (Generic)	$T_{MIR} > 317$ K (day) $T_{TIR} > 295$ K (night) (applied only within forest mask to reject false detections due to solar heated soil, which could approach saturation).	AVHRR (Forest fires - Spain)
Justice and Dowty (1994)	Contextual (3)	$T_{MIR-t} > 316$ K $T_{TIR-t} > 290$ K $T_{TIR-t} < T_{MIR-t}$ NOW, Target pixel $\Delta T > \Delta T$ mean from the background, plus two times the standard deviation of the ΔT for the background pixels … … … or 3 K (whichever is greater).	Algorithm developed at NASA/Goddard Space Flight Centre
Prins and Menzel (1994)	Contextual	Estimate the mean and standard deviation in T_{MIR} and T_{TIR} for all cloud-free pixels across a 150 km × 150 km sector. This defines the background values for each band (T_{MIR-b} and T_{TIR-b}); NOW: $\Delta T_t >$ mean ΔT_b $T_{MIR-t} - T_{MIR-B} > 1.5\ \sigma(T_{MIR-B})$ $T_{MIR-t} > 300$ K and $T_{TIR-t} > 295$ K $T_{TIR-t} - T_{TIR-b} > 1$ K $T_{MIR-t} - T_{MIR-b} > 5$ K $T_{fire}^{*} > 400$ K	GOES-VAS (Burning – S. America)
Arino and Melinotte (1995)	Fixed (Generic)	$T_{MIR} > 320$ K (saturation test); $T_{MIR} > T_{TIR} + 15$; $T_{TIR} > 245$ K (cloud test); $R_{VIS} < 25$ % (reflection test); $R_{VIS} - R_{NIR} > 1$ % (sunglint test).	AVHRR (Fires – Africa)
Franca et al. (1995)	Fixed (Generic)	$T_{MIR} > 320$ K $\Delta T > 15$ K $T_{TIR} > 287$ K $0 \leq T_{10\mu m} - T_{12\mu m} \geq 5$ K $R_{VIS} < 9$ %	AVHRR (Wild fires – West Africa)
Flasse and Ceccato (1996)	Contextual (3)	$T_{MIR} > 311$ K $\Delta T > 8$ K $T_{MIR} - [\text{mean } T_{MIR-b} - 2\sigma] > 3$ K $\Delta T > [\text{mean } \Delta T_b - 2\sigma]$	

[§] http://www.cambridge.org/us/academic/subjects/earth-and-environmental-science/remote-sensing-and-gis/thermal-remote-sensing-active-volcanoes-users-manual

(1) The algorithm was also applied for fire detection in AVHRR data for West Africa by Kennedy et al. (1994).

(2) Another algorithms was published with a similar basis, but using DN criteria (fire if DN < 10 or 8, i.e., if DN are close to AVHRR saturation), by Pereira and Setzer (1993).

(3) Algorithm uses 9 × 9 pixel box centered on background cleaned of potential fire pixels; box expanded up to limit of 21 × 21 pixels until at least 25 % of pixels are non-fire.

*estimated using the dual-band method of Dozier (1981).

T_{MIR} = Mid-infrared pixel-integrated temperature; T_{TIR} = Thermal-infrared pixel-integrated temperature;
$T_{10\mu m}$ = Pixel-integrated temperature at 10 μm; $T_{12\mu m}$ = Pixel-integrated temperature at 12 μm;
$T_{MIR\text{-}t}$ = Target pixel MIR brightness temperature; $T_{MIR\text{-}b}$ = Background pixel MIR brightness temperature;
$T_{TIR\text{-}t}$ = Target pixel TIR brightness temperature; $T_{TIR\text{-}b}$ = Background pixel TIR brightness temperature;
$\Delta T = T_{MIR} - T_{TIR}$; T_{fire} = sub-pixel fire temperature; T_{thresh} = threshold temperature; σ = standard deviation
R_{NIR} = Near-infrared reflection; R_{VIS} = Visible reflection; DN = Digital Number (subscripts as per temperatures)

Table 3. Data archiving at NEODAAS-Dundee began in 1978 with the launch of TIROS-N. Today the archive includes data from 10 sensors flown on polar orbiter and geostationary platforms. While a collation of all AVHRR archive data spanning effusive eruptions at Etna are given in Harris et al. (2011); those for Krafla (Iceland) are given in Harris et al. (2000a).

Satellite - sensor	Archive temporal coverage	Source
NPP VIIRS	July 2012 - present	NEODAAS-Dundee
Aqua/Terra MODIS	Apr. 2000 - present	NEODAAS-Dundee & NASA
NOAA/METOP AVHRR	Nov. 1978 - present	NEODAAS-Dundee
Nimbus-7 CZCS	Aug. 1979 - Jun 1986	NEODAAS-Dundee
OrbView-2 SeaWiFS	Sept. 1997 - Dec 2010	NEODAAS-Dundee
Envisat MERIS	2004 - 2012	ESA
Geostationary satellites[1]	2001-present	NEODAAS-Dundee, ESA & NOAA

[1] SEVIRI, VISSR, GOES and MTSAT

Table 4. Locations of, and average transmissivities, $\tau(\lambda)$, across, the seven main atmospheric windows in the NIR, MIR and TIR (adapted from Harris, 2013). Values obtained using MODTRAN applied using a 1976 US Standard atmosphere with a vertical path from sea-level to space (zenith = 180 °, observer height = 100 km), a CO_2 mixing ratio of 380 ppm·v. In the final column is the range of temperatures (T_{peak}) which have their peak of spectral exitance (λ_m) in the given waveband following re-arrangement of Wien's displacement law, i.e., $T_{peak} = 2898\ \mu m\ K / \lambda_m$.

Window Location	Waveband (μm)	Width (μm)	Average $\tau(\lambda)$	Max $\tau(\lambda)$	Location of Max $\tau(\lambda)$ (μm)	T_{peak} (°C)
NIR	0.7 to 0.89	0.19	0.90	0.93	0.89	3900 to 3000
NIR	1.0 to 1.1	0.1	0.94	0.95	1.07	2600 to 2300
SWIR	1.18 to 1.31	0.13	0.94	0.96	1.25	2200 to 1900
SWIR	1.51 to 1.76	0.25	0.96	0.97	1.68	1650 to 1400
SWIR	2.03 to 2.36	0.33	0.96	0.98	2.14	1150 to 950
MIR	3.44 to 4.13	0.69	0.94	0.97	3.96	570 to 430
TIR	8.6 to 12.2	3.6	0.92	0.96	10.11	64 to -35

Table 5. Tests and thresholds used by Harris et al. (2001a) to estimate of hot spot probability. Values output by the algorithm are scaled to 0 to 1, where negative values are mapped to the range 0-0.5 (i.e. 0-50 % probability) and positive values are mapped to the range 0.51-1 (i.e. 51-100 % probability).

Probability step (label)	Test	Description
1 (Prob 1)	Brightness	Pixel albedo (A1) is compared with an albedo threshold ($\tau 1$) to determine the probability that the pixel is cloud-covered: Bright pixels (i.e., A1 > $\tau 1$) are given a positive weighting dependent on the magnitude of the A1 - $\tau 1$ difference. Non-bright values (i.e., A1 < $\tau 1$) are given a negative weighting dependent on the A1 - $\tau 1$ difference.
2 (Prob 2)	Thermal difference	Pixel ΔT radiance is compared with its background (as characterized by the mean of neighboring pixels in a 25 × 25 pixel box centered on the target pixel = $\Delta TBck$). This provides a measure of the thermal difference between a pixel and its immediate background. If $\Delta T > \Delta TBck$, then the pixel is given a positive weighting dependent on the magnitude of the $\Delta T - \Delta TBck$. Difference. If $\Delta T < \Delta TBck$ then the pixel is given a negative weighting dependent on the magnitude of the ΔT 1 - $\Delta TBck$ difference.
3 (Prob 2-4)	Thermal anomaly	Pixel ΔT is compared with a ΔT threshold of 10 ºC (ΔTthresh). This gives a measure of thermally anomalous activity. If $\Delta T > \Delta T$thresh, then the pixel is given a positive weighting dependent on the magnitude of the $\Delta T - \Delta T$thresh difference. If $\Delta T < \Delta T$thresh, then the pixel is given a negative weighting dependent on the magnitude of the $\Delta T - \Delta T$thresh difference.
4 (Prob 4)	Cold test	Pixel TIR brightness temperature (TIR) is compared with a TIR temperature threshold (τTIR), which corresponds to a pixel brightness temperature of -23ºC. This gives a measure of how cold the pixel is, and thereby the probability that cold cloud is present. If TIR > τTIR, then the pixel is given a positive weighting dependent on the magnitude of the TIR – τTIR difference. If TIR < TIR, then the pixel is given a negative weighting dependent on the magnitude of TIR – τTIR difference.
Total probability (PROB)	PROB = Prob 1 × Prob 2 × Prob 3 × Prob 4	Total probability is the product of the 4 sub-probabilities (Prob 1 to 4) and is therefore designed to provide a quantitative assessment of whether a pixel (1) contains cloud, (2) is thermally different from its background, and (3) is thermally anomalous.

Table 6. AVHRR-derived TADR log built during Etna's 2001 flank eruption.

Date	Time (GMT)	TADR Max ($m^3 s^{-1}$)	TADR Min ($m^3 s^{-1}$)	Notes
16 July 2001	00:47	2 pixels @ SEC		
16 July 2001		--	--	Scan Edge
16 July 2001		--	--	Cloud
16 July 2001		--	--	Cloud
17 July 2001	00:37	16 pixels @ SEC		
17 July 2001	02:19	--	--	Scan Edge
17 July 2001	12:13	8 pixels @ SEC		Wrap round
17 July 2001	16:07	--	--	Cloud
18 July 2001	02:08	--	--	Cloud
18 July 2001	12:10	16.1	8.8	1st w/2100m hot spot
19 July 2001	01:50	10.1	4.4	
19 July 2001	11:59	21.8	11.9	
19 July 2001	13:40	--	--	Scan Edge
21 July 2001	01:29	--	--	Wrap Round
21 July 2001	11:39	--	--	Scan Edge
21 July 2001	13:19	27.7	13.7	
21 July 2001	16:18	28.1	12.2	
22 July 2001	01:19	30.0	12.0	
22 July 2001	11:28	--	--	Scan Edge
22 July 2001	13:09	19.3	9.1	
22 July 2001	15:55	22.0	9.2	
23 July 2001	01:09	31.8	12.6	
23 July 2001	12:58	--	--	Wrap Round
23 July 2001	15:32	20.7	8.9	
24 July 2001	00:58	24.9	10.0	
24 July 2001	05:05	6.6	2.8	
24 July 2001	12:48	--	--	Wrap Round
25 July 2001	00:47	23.3	9.6	
25 July 2001	12:37	--	--	Cloud
25 July 2001	16:25	--	--	Cloud
26 July 2001	00:37	--	--	Cloud
26 July 2001	02:17	--	--	Scan Edge
26 July 2001	12:27	--	--	Cloud
27 July 2001	00:27	10.8	4.5	
27 July 2001	02:07	--	--	Scan Edge
27 July 2001	12:16	--	--	Cloud
28 July 2001	01:56	12.2	5.1	
28 July 2001	12:06	--	--	Cloud
29 July 2001	01:46	14.2	5.9	
29 July 2001	11:55	--	--	Cloud
29 July 2001	13:36	--	--	Cloud
29 July 2001	16:32	--	--	Cloud
30 July 2001	01:36	19.1	8.0	
30 July 2001	11:45	--	--	Cloud
30 July 2001	13:26	26.2	13.4	
30 July 2001	16:09	26.2	12.5	
31 July 2001	01:25	20.0	8.3	
31 July 2001	11:34	--	--	Cloud
31 July 2001	13:20	--	--	Cloud
31 July 2001	15:46	--	--	Cloud
1 August 2001	01:15	--	--	Plume
1 August 2001	05:19	--	--	Plume & Scan Edge
1 August 2001	11:24	--	--	Scan Edge
1 August 2001	13:05	--	--	Plume
2 August 2001	01:04	--	--	Plume
2 August 2001	12:54	--	--	Plume
2 August 2001	16:39	--	--	Plume
3 August 2001	00:54	3.1	7.7	
3 August 2001	12:44	--	--	Cloud
3 August 2001	16:16	--	--	Cloud
4 August 2001	00:43	--	--	Plume
4 August 2001	02:24	--	--	Scan Edge

4 August 2001	12:33	--	--	Plume
5 August 2001	00:33	2.5	5.8	
5 August 2001	02:13	--	--	Scan Edge
5 August 2001	05:26	--	--	Scan Edge
5 August 2001	12:23	6.4	13.6	
6 August 2001	00:23	1.8	4.1	
6 August 2001	02:03	--	--	Scan Edge
6 August 2001	12:12	--	--	Cloud
6 August 2001	16:46	--	--	Scan Edge
7 August 2001	01:52	1.0	2.4	
7 August 2001	12:02	3.7	8.7	
7 August 2001	13:42	--	--	Scan Edge
7 August 2001	16:23	--	--	Cloud
8 August 2001	00:43			Minor plume to SE
8 August 2001	11:51	--	--	Cloud: no plume
8 August 2001	13:32	--	--	Cloud: no plume
8 August 2001	16:00	--	--	Cloud: no plume
9 August 2001	01:31	1.2	2.8	
9 August 2001	11:14	0.3	0.6	
9 August 2001	13:21	--	--	Cloud
9 August 2001	15:36	--	--	Cloud

Table 7. Activity time-line and AVHRR observations for Etna during July 1 – 18, 2001.

Date	Ground-based observations (INGV-Catania)	AVHRR-based observations
July 1-4	No glow observed (last paroxysm from SEC was ~23:00 (6/29) - ~21:00 (6/30)	1-3 pixel, low magnitude hot spots @ SEC
July 4	11:00: lava effusion begins @ SEC 22:30: Increase in Strombolian activity 00:45: Activity declining (07/5)	8 pixel, high magnitude hot spot @ SEC
July 7-17	Continuous lava flow effusion from SEC	AVHRR hot spot steadily increases in size and magnitude: 7/07 = 2 pixels 7/11 = 3 pixels 7/15 = 6 pixels
July 9	Episode of mild strombolian activity @ SEC (early)	AVHRR = cloud covered
July 13	Paroxysm @ SEC (early am)	01:19 GMT image shows 3 pixel, high magnitude hot spot at SEC
July 17	Paroxysms @ SEC in early am, in the following hours fissures open at the S. base of SEC and extend S. These feed strombolian & lava flow activity	00:37 GMT image shows 16 pixel, high magnitude anomaly @ SEC with plume extending ENE. 12:13 GMT image shows high magnitude hot spot between SEC and Montagnola
July 17	Second fissure becomes active on N flank of Montagnola. Flows begin to extend away from eruptive fissure. Over the following days these flow extended S to threaten the ski area and Sapienza complex	
July 18	~02:00 (local time) 2100 m vent begins activity. Over following days flows from this vent extend S towards Nicolosi	12:03 GMT image shows first dual hot spot, with hot spot #1 between SEC and Montagnola, & #2 below Montagnola (2100 m vent)
July 18	Main vent on N flank of Montagnola opens up: becomes source of major ash emissions	
July 20	Flow active from NE extending fissure segment, flows extend into Valle del Leone	Activity apparent as third hot spot to NE of SEC especially on July 22-23 images

Table 8. Email notices sent out between 19 March and 9 April during Stromboli's 2007 eruption.

To: Distribution list Re: Stromboli: 19-28 March 2007
Complete or partial cloud cover meant that no AVHRR-based TADR estimates were possible during 18-25 March (although the anomaly was observed through or between clouds on 10 occasions). Since 26 March cloud conditions have improved allowing TADR estimates from 5 of the 14 passes over the last 3 days. These give the following TADRs: 26 March 07 – 09:54 UT – 0.9 – 1.4 m^3/s 26 March 07 – 12:21 UT – 0.7 – 1.6 m^3/s 27 March 07 – 21:00 UT – 0.7 – 1.7 m^3/s 28 March 07 – 12:01 UT – 0.7 – 1.6 m^3/s 28 March 07 – 20:37 UT – 0.5 – 1.4 m^3/s
To: Distribution list Re: Stromboli: 28 March – 3 April 2007
Complete or partial cloud cover meant that no AVHRR-based TADR estimates were possible during 29 & 30 March. Since the afternoon of 31 March cloud conditions have improved allowing TADR estimates from 4 passes spanning 31 March – 2 April. These give the following TADRs: 31 March 07 – 21:08 UT – 0.5 – 1.3 m^3/s 01 April 07 – 01:24 UT – 0.4 – 0.9 m^3/s 01 April 07 – 20:45 UT – 0.9 – 2.2 m^3/s 02 April 07 – 12:50 UT – 0.6 – 1.3 m3/s As of 3 April, cloud conditions had deteriorated again such that all 5 of today's images were cloud covered.
To: Distribution list Re: Stromboli: 3-9 April 2007
Although we've looked at data from 34 passes during 3-9 April, cloud (sometimes localized but just sitting right over Stromboli) has meant that we have had no data suitable for TADR calculation since 2 April. We did see a band 3 hot spot on 5 occasions in this period, but they all appeared cloud contaminated and there was no convincing band 4 anomaly.